Atmósfera 40, 127-151 (2026)
https://doi.org/10.20937/ATM.53524

Superrotation of the Venus' atmosphere computed with a thermodynamic model

Víctor M. MENDOZA[1], Blanca MENDOZA[2], Marni PAZOS[1]*,
Arturo I. QUINTANAR[1] and René GARDUÑO[1]

[1] *Instituto de Ciencias de la Atmósfera y Cambio Climático, Universidad Nacional Autónoma de México, Circuito de la Investigación Científica s/n, Ciudad Universitaria, 04510 Ciudad de México, México.*
[2] *Instituto de Geofísica, Unidad Michoacán, Universidad Nacional Autónoma de México, 58089 Morelia, Michoacán, México.*
*Corresponding author; email: marni@unam.mx

Received: July 28, 2025; Accepted: February 12, 2026

RESUMEN

Se desarrolló un modelo termodinámico que subordina la dinámica de la superrotación atmosférica de Venus a los forzamientos térmicos. El mecanismo clave es una marea térmica diurna, generada por un calentamiento simplificado basado en el equilibrio radiativo entre la insolación solar y la emisión de onda larga. Este calentamiento produce gradientes horizontales de temperatura (día-noche y ecuador-polo) que, a través del equilibrio hidrostático, se traducen en gradientes de geopotencial. Dichos gradientes actúan como la fuerza principal en las ecuaciones de movimiento, incrementando el momento angular específico con la altitud y generando un viento zonal superrotante en la dirección de la rotación planetaria, pero opuesto a la lenta propagación de la marea térmica. La integración numérica en 24 capas troposféricas, junto con un modelo de conductividad térmica del regolito (hasta 19.1 m de profundidad) para calcular el flujo de calor superficial, muestra que la circulación vertical inducida térmicamente transporta el momento angular desde la superficie hacia el nivel de las nubes. Se concluye que la marea térmica diurna, impulsada por los gradientes de insolación, es el mecanismo fundamental que genera y mantiene la superrotación en la atmósfera de Venus. Este enfoque termodinámico novedoso proporciona un marco unificado para comprender este fenómeno en planetas de rotación lenta.

ABSTRACT

A thermodynamic model is developed in which the dynamics of Venusian atmospheric superrotation is subordinated to thermal forcing. The key mechanism is a diurnal thermal tide, generated by simplified heating based on radiative balance between solar insolation and long-wave emission. This heating produces horizontal temperature gradients (day-night and equator-pole), which, through hydrostatic equilibrium, translate into geopotential gradients. These gradients act as the primary force in the equations of motion, increasing specific angular momentum with altitude and generating a superrotating zonal wind in the direction of planetary rotation, but opposed to the slow propagation of the thermal tide. Numerical integration across 24 tropospheric layers, coupled with a regolith thermal conductivity model (down to 19.1 m depth) to compute surface heat flux, demonstrates that thermally induced vertical circulation transports angular momentum from the surface to the cloud level. It is concluded that the diurnal thermal tide, driven by insolation gradients, is the fundamental mechanism generating and maintaining superrotation in Venus' atmosphere. This novel thermodynamic approach provides a unified framework for understanding this phenomenon on slowly rotating planets.

Keywords: Venus' atmosphere, planetary atmospheres, Venus' superrotation.

1. Introduction

Venus is the second rocky planet from the Sun (0.72 AU). Its atmosphere is a mixture of gases with 96.5% carbon dioxide (CO_2), 3.5% molecular nitrogen (N_2), 0.015% sulfur dioxide (SO_2), 0.007% argon (Ar), ~0.002% water vapor (H_2O), and other chemical compounds in smaller amounts. This mixture gives a molecular weight of 43.44 g mol^{-1}, close to that of CO_2. Venus has the most massive atmosphere among the terrestrial planets in the Solar System, exerting a surface pressure of 9.2×10^6 Pa, 91 times greater than that of the Earth's atmosphere. The surface density and surface average temperature of Venus are 65 kg m^{-3} and 737 K, respectively (Gulkis and de Pater, 2003; Taylor and Hunten, 2014).

The troposphere of Venus is ~70 km thick and contains 99% of the total atmospheric mass. It also includes a cloud layer between ~48 and 70 km altitude that completely envelopes the planet. It has been established that the clouds were primarily composed of sulfuric acid (H_2SO_4) droplets, contributing significantly to the planet's high albedo of 76% (Moroz et al., 1985; Titov et al., 2007; Lebonnois et al., 2010). However, a recent reanalysis of the Pioneer Venus mission datasets, published by Mogul et al. (2025), proposes that cloud aerosols are not predominantly composed of concentrated H_2SO_4, as previously hypothesized, but rather contain approximately 60% water by mass. This significant water fraction appears to be sequestered within hydrated sulfate salts, likely involving iron and magnesium cations, potentially sourced from meteoric dust.

Venus has a mean radius of a = 6051.3 km, very close to the mean radius of the Earth, and rotates on its axis with an angular velocity $\Omega = 2.98 \times 10^{-7}$ s^{-1}, two orders of magnitude smaller than that of the Earth. Its rotational period is ~243 Earth days, longer than its orbital period of 224.7 Earth days. Its atmosphere rotates in the same direction as the solid planet, but at cloud level it rotates 60 times faster, with zonal winds reaching speeds exceeding 100 m s^{-1}. This phenomenon is known as superrotation and is one of the most conspicuous phenomena in Venus' atmosphere that is not yet fully understood (Titov et al., 2007; Sánchez-Lavega et al., 2017).

Similar to Earth, the energy that drives the circulation of Venus' atmosphere is solar radiation. Consequently, an unresolved issue is to quantitatively explain how radiant energy is transformed into the atmosphere's mechanical energy, particularly regarding superrotation. In trying to find answers to this problem, researchers have used general circulation models (GCMs) (e.g., Yamamoto and Takahashi, 2003a; Lee et al., 2007; Mendonça and Read, 2016; Takagi et al., 2018; Sugimoto et al., 2019) and have looked at the role that waves and turbulence have in maintaining superrotation (Takagi and Matsuda, 2007; Kouyama et al., 2019).

To give a physically plausible explanation for the maintenance of superrotation, Matsuda (2010) mentions three possible mechanisms based on: (a) the circulation between day and night (diurnal circulation) due to the prolonged insolation that Venus receives during its solar day (Venus day) of ~117 Earth days (Schubert and Whitehead, 1969); (b) momentum transport associated with the vertical propagation of thermal tides excited by solar heating in the cloud layer (Fels and Lindzen, 1974; Takagi and Matsuda, 2007); and (c) meridional circulation and angular momentum transported upward and poleward (Gierasch, 1975; Rossow and Williams, 1979; Matsuda, 1980, 1982).

Takagi and Matsuda (2007) addressed mechanism (b) by means of a GCM where diurnal and semi-diurnal thermal tides excited by solar heating generate and maintain the atmospheric superrotation of Venus through momentum transport; the superrotation extends from the surface up to 80 km altitude with a vertical profile similar to the observations (Fujisawa et al., 2022). The assimilation of data from the Akatsuki orbiter improved the view of the three-dimensional structures of thermal tides and found that they play a crucial role in maintaining the superrotation of the Venusian atmosphere.

Sugimoto et al. (2023) conducted simulations using a Venus atmospheric GCM at medium and high resolutions, exploring a range of horizontal diffusion strengths. They found that fully developed super-rotation could be maintained across a specific range of diffusion values, indicating that its structure is largely independent of horizontal diffusion within that range.

Previous numerical studies with GCMs (Takagi and Matsuda, 2007; Titov et al., 2007; Takagi et al., 2018; Kouyama et al., 2019) have also shown the importance of thermal tides in maintaining the superrotation of Venus' atmosphere, which plays an important role in the transport of angular momentum balance. For example, Fukuya et al. (2021) found that the semidiurnal tide has a large enough amplitude to contribute significantly to the maintenance of superrotation. Yamamoto and Takahashi (2003b) conducted a study that reproduced significant atmospheric superrotation with zonal velocities exceeding 100 m s^{-1} at the cloud-top level (~70 km), characterized by a strong meridional circulation in a single cell extending from the surface to approximately 80 km above the clouds. The authors also incorporated a dominant process into their superrotation model, employing the generation mechanism proposed by Gierasch (1975), which involves the angular momentum balance between mean meridional circulation and wave transport (mechanism c) (Matsuda, 2010).

Yamamoto and Takahashi (2007) demonstrated that vertical eddy diffusion plays a crucial role in shaping the dynamics of Venus' atmosphere, especially in sustaining superrotation. Cohen et al. (2025) employed the Venus Planetary Climate Model and data from the Pioneer Venus probes to identify three distinct atmospheric circulation regimes, each occurring at different altitudes and associated with varying rotation rates.

Regarding thermodynamic models, Takahashi et al. (2024) examined how the radiative-convective equilibrium structure of Venus' lower atmosphere depends on various atmospheric thermodynamic models. They concluded that employing an ideal gas model with a temperature-dependent specific heat that reproduces the adiabatic lapse rate profile of real gases is a promising approach.

In any case, the actual thermodynamic and dynamic mechanism by which the superrotation of Venus' atmosphere is generated and maintained is not entirely clear.

The purpose of this work is twofold: (1) to present a simplified global thermodynamic model where the dynamics is subordinated to thermodynamics, and (2) to provide a theoretical explanation of how the horizontal gradients of the geopotential play an important role in establishing and maintaining the global circulation of Venus' atmosphere, especially the superrotation, due to the differential heating of the solar radiation between day and night (zonal gradient) and between the equator and the poles (meridional gradient).

2. Method and model description

The atmospheric and surface temperatures are computed using conservation of thermal energy applied to the tropospheric and surface regolith layers. The tropospheric layer includes a cloud cover enveloping the entire planet. The equations of atmospheric motion are obtained in pressure coordinates, assuming a constant temperature lapse rate and hydrostatic equilibrium, and using the ideal gas equation; the geopotential can be expressed as a function of the pressure coordinate and the atmospheric temperature at the surface. The regolith surface-layer temperature is obtained using the thermal conductivity equation as a function of the atmospheric surface temperature and the regolith subsurface-layer temperature.

2.1 The tropospheric thermodynamic equation

The tropospheric temperature is obtained by vertically integrating the conservation of thermal energy equation for a column of unit area from the surface to the Venus tropospheric top at ~70 km. The atmosphere includes a planetary cloud cover with a thickness of ~22 km, between 48 and 70 km altitude. The corresponding energy balance can be expressed in a similar way as has been applied to the Earth's atmosphere (Adem, 1965):

$$\int_0^H \langle\rho^*\rangle c_v \ \partial\frac{\langle T^*\rangle}{\partial t}dz + \int_0^H \Big(\langle\rho^*\rangle c_v \ \nabla\bullet\left\langle V^{*\prime\prime}T^{*\prime\prime}\right\rangle + c_v \left\langle V^{*\prime\prime}\,T^{*\prime\prime}\right\rangle\bullet\nabla\ \langle\rho^*\rangle\Big)dz = \left\langle E_T\right\rangle + \left\langle G_2\right\rangle \tag{1}$$

where the superscript (*) indicates variables that depend on altitude (z), horizontal coordinates, and time; ⟨ ⟩ represents space and time average values; (") in the horizontal velocity vector and in the temperature represents the turbulence and fluctuation of velocity and temperature with respect to their time-averaged values, respectively; H is the thickness of the troposphere; ρ^* is the density; c_v is the specific heat at constant volume; T^* is the temperature; t is the time, V^* is the horizontal wind velocity, and ∇ is the horizontal gradient operator in two dimensions. The term $\langle\rho^*\rangle c_v\langle T^*\rangle$ is the thermal energy storage per unit of volume; $\nabla\cdot(\langle\rho^*\rangle c_v \langle V^{*\prime\prime} T^{*\prime\prime}\rangle)$ is the divergence of the horizontal turbulent transport of thermal energy corresponding to the sum of the two terms of the second integral; and $\langle E_T \rangle$ and $\langle G_2 \rangle$ represent the rate at which the thermal energy is added to the vertical column due to radiation and vertical turbulent transport of sensible heat from the surface.

To simplify the thermodynamic model, in Eq. (1) we have not considered the transport of thermal energy by horizontal wind and vertical currents; however, we believe that its incorporation can appreciably modify the temperature field, initiating a non-negligible feedback process between thermodynamics and the dynamics of the atmosphere. Additionally, we neglected the vertical turbulent transport of thermal energy at the top of the atmosphere, which includes the rate at which the thermal energy increases due to heat transfer by molecular conduction and friction, and the rate at which the thermal energy increases in the column due to work done by compression on the column. Moreover, Eq. (1) does not include the latent heat released by condensation since we assume that it is used to evaporate the H_2SO_4 raindrops before they reach the surface.

We further assume that horizontal turbulent heat transport occurs in the opposite direction to the temperature gradient, which can be expressed as:

$$\langle V^{*''} T^{*''} \rangle = -K \, \nabla \langle T^* \rangle \tag{2}$$

where K is the turbulent exchange coefficient (Austausch coefficient), which is considered constant.

We consider the troposphere to be an ideal gas in hydrostatic equilibrium with a constant temperature lapse rate Γ. To have temperature fields in terms of pressure coordinates, we assume that the acceleration of gravity g remains constant between the equator and the poles and between the surface and the top of the troposphere at $z = H$; then, the geopotential Φ^* can be approximated as $\Phi^* = gz$. In this way, the planet's average surface at $z = 0$ results in an equipotential surface or constant geopotential surface $\Phi^* = 0$. Therefore, assuming a constant temperature lapse rate Γ, the temperature field $\langle T^* \rangle$ can be expressed as:

$$\langle T^* \rangle = T_s - \gamma \Phi^* \tag{3}$$

where T_s is the surface atmospheric temperature at $\Phi^* = 0$ and $\gamma = \Gamma / g$. Assuming an atmosphere in hydrostatic equilibrium and using the equation of state and Eq. (3), the hydrostatic equilibrium equation can be expressed as:

$$\mathrm{p}^* \frac{\partial \Phi^*}{\partial p^*} - R\gamma \Phi^* = -R T_s \tag{4}$$

where R is the gas constant. The solution of Eq. (4) is given by:

$$\Phi^*(\lambda, \varphi, p^*, t) = \frac{1}{\gamma} \left[1 - \left(\frac{p^*}{p_s} \right)^{R\gamma} \right] T_s(\lambda, \varphi, t) \tag{5}$$

Eq. (5) expresses the geopotential Φ^* (λ, φ, p^*, t) as a function of the longitude λ latitude φ and, explicitly, the pressure p^* as a vertical coordinate and time t. The temperature T_s (λ, φ, t) is only a function of λ, φ and t. In (5) p_s is the isobaric surface, which coincides with the surface of Venus, and where, according to (5), the geopotential is zero. From now on, Φ^* (λ, φ, p^*, t) will be simply expressed as Φ^*, the same for the other variables of the model.

Substituting (5) into (3), we obtain the temperature in pressure coordinates:

$$\langle T^* \rangle = T_s \left(\frac{p^*}{p_s} \right)^{R\gamma} \tag{6}$$

where $\langle T^* \rangle$ is the temperature on the isobaric surface p^* and T_s is the temperature $\langle T^* \rangle$ at the isobaric surface p_s. To compute $R\gamma = R\Gamma/g$, we use $g = 8.87$ m s^{-2} as the acceleration of gravity and R = 191.1 JKg^{-1}K^{-1}, computed using an average molecular weight of 43.5 g mol^{-1} (Petropoulos and Telonis, 1993). We use $\Gamma = 7.64 \times 10^{-3}$ km^{-1}, an average of the Venera profiles 8, 9, and 10, and the Pioneer Venus profile (Schubert et al., 1980; Fig. 2). This value is very close to that obtained with the profile of the Venus International Reference Atmosphere Model (VIRA), where the troposphere only presents instability in the first 5 km, between 17 and 20 km, and at cloud level between 50 and 55 km; the rest of the troposphere is stable (Titov et al., 2007).

Using Eq. (6), $\langle T^* \rangle$ can be expressed in terms of the mean tropospheric temperature T_m, defined in the model as the temperature in $p_m = p_s/2$. Above and below this isobaric surface, half of the atmospheric mass is located, so it is an appropriate level for defining a mean tropospheric temperature:

$$\langle T^* \rangle = T_m \left(\frac{p^*}{p_m} \right)^{R\gamma} \tag{7}$$

We substitute Eq. (7) in the integrals of Eq. (1), considering that H is the altitude of the isobaric surface where the troposphere ends. Such surface corresponds to $p = 3.6\times10^3\ Pa$ (~70 km). Neglecting the orographic effects, we assume that Venus' surface pressure corresponds to $p_s = 9.2 \times 10^6$ Pa; in this way, $p_m = 4.6 \times 10^6\ Pa$ (~10.5 km).. Therefore, considering the equation of hydrostatic equilibrium $dz = -dp^*/\langle\rho^*\rangle g$, Eq. (1) can be integrated from p_s up to p, giving the following expression:

$$F_2\left(\frac{\partial T'_m}{\partial t} - K\,\nabla^2 T'_m\right) = E_T + G_2 \tag{8}$$

Here, we used the parameterization from Eq. (2) for the third integral, neglecting the integral of the turbulent transport term, $c_v\,\langle V^{*\prime\prime}\,T^{*\prime}\rangle\cdot\nabla\langle\rho^*\rangle$. This hypothesis has also been applied to Earth's atmosphere (Adem, 1970). In Eq. (8), $T'_m = T_m - Tm_0$ is the temperature perturbation of T_m, and Tm_0 is a constant. Introducing T'_m linearizes the net tropospheric radiative heating E_T and the vertical turbulent sensible heat flux G_2, such that Eq. (8) corresponds to a second-degree linear differential equation. To simplify, we denote the average values $\langle E_T\rangle$ and $\langle G_2\rangle$ by E_T and G_2, respectively, where F_2 is given by:

$$F_2 = \frac{c_v p_s}{g}\frac{1}{1+R_\gamma}\left[\left(\frac{p_s}{p_m}\right)^{R\gamma} - \left(\frac{p}{p_m}\right)^{R\gamma}\left(\frac{p}{p_s}\right)\right] \approx \frac{c_v p_s}{g}\frac{1}{1+R\gamma}\left(\frac{p_s}{p_m}\right)^{R\gamma} \tag{9}$$

where the approximation is due to $\left(\frac{p}{p_s}\right) \ll 1$.

2.2 Radiation balance

Assuming that the Venus atmosphere is composed of 96.5% CO_2, which is well mixed in the troposphere, we have calculated, as in Mendoza et al. (2017, 2021), the emissivity ϵ_a of the Venus troposphere using the spectral calculator E-TRANS, with the database HITRAN (Rothman et al, 2009), finding that $\epsilon_a = 0.94$, which is almost a black body emissivity:

$$E(T^*) = \epsilon_a \sigma \tag{10}$$

Here, σ is the Boltzmann constant, and $E(T^*)$ is the energy per unit area and time emitted by the tropospheric horizontal borders, being only a function of the temperature (for simplicity $\langle T^*\rangle$ is written as T^*). We assume that the emissivity of the atmospheric layers above the troposphere does not contribute to the radiation balance and, therefore, is not considered. Also, we assume that the cloud cover emits as a black body with a lower boundary at ~48 km and an upper boundary at ~70 km, which coincides with the upper tropospheric boundary. The same assumption is made for the regolith surface.

We define T_{C_1} as the temperature of the cloud cover's lower boundary, and we assume it to be equal to the tropospheric temperature at that level. Similarly, T_{C_2} is the cloud cover temperature at the upper boundary, assumed to be equal to the tropospheric temperature at that level. Finally, T_s is the surface atmospheric temperature. These temperatures can be calculated in terms of T_m using Eq. (7): +

$$\begin{aligned} T_s &= T_m\left(\frac{p_s}{p_m}\right)^{R\gamma} \\ T_{C_1} &= T_m\left(\frac{p_c}{p_m}\right)^{R\gamma} \\ T_{C_2} &= T_m\left(\frac{p}{p_m}\right)^{R\gamma} \end{aligned} \tag{11}$$

where $p_C = 1.4 \times 10^5$ Pa (~48 km) is the lower cloud cover boundary pressure.

Figure 1 shows the model's radiation balance scheme, similar to that on Earth (Adem, 1962); however, on Venus, the cloud cover is complete, while on Earth it is partial. In this figure, we notice that

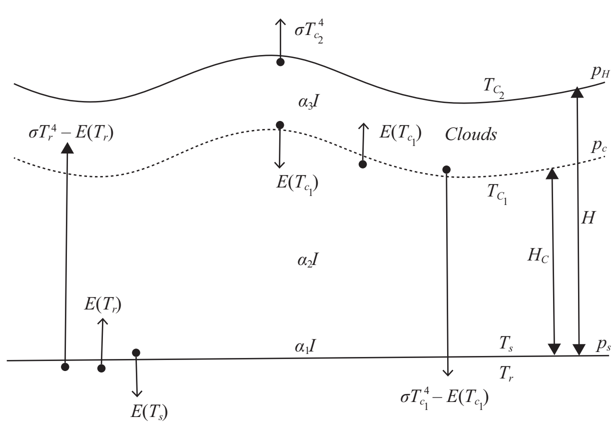

Fig. 1. Representation of the radiation balance of the Venus troposphere with a cloud layer covering the entire planet. In this figure, T_r is the surface temperature of regolith.

per unit area and time, the regolith surface absorbs solar radiation $\alpha_1 I$, the troposphere $\alpha_2 I$, and the cloud cover $\alpha_3 I$, with the fractions α_1, α_2 and α_3 related to the planetary albedo α_p through:

$$\alpha_P I = \left[1 - \left(\alpha_1 + \alpha_2 + \alpha_3\right)\right] I \quad (12)$$

where I is the insolation or solar radiation arriving at the planetary surface per unit area and time in the absence of atmosphere, computed with the Milanković formula (Milanković, 1920) using the Venus orbital parameters from Archinal et al (2018). Figure 2 shows the solar radiation I (W m^{-2}) at the beginning of a Venusian day, whose maximum intensity of 2566.5 is centered on longitude 0º E on the equator, advancing in the west-east direction and returning to the same position after ~117 Earth days, when the sunrise is at 90º E.

Following Titov et al. (2007), we use constant values for α_1, α_2 and α_3: $\alpha_1 = 0.032$, $\alpha_2 = 0.048$, and $\alpha_3 = 0.16$, such that using Eq. (12), the planetary albedo is $\alpha_p = 0.76$

According to Figure 1, the radiation balance (the difference between the incoming and outgoing energies) in the troposphere, including the radiation balance in the clouds, is expressed as:

$$E_T = \sigma T_r^4 + \left(\alpha_2 + \alpha_3\right) I - E\left(T_s\right) - \sigma T_{C_2}^4 - \left[\sigma T_{C_1}^4 - E\left(T_{C_1}\right)\right] \quad (13)$$

where T_r is the surface temperature of the regolith. The radiation balance at the surface E_r is:

$$E_r = E\left(T_s\right) + \left[\sigma T_{C_1}^4 - E\left(T_{C_1}\right)\right] + \alpha_1 I - \sigma T_r^4 \quad (14)$$

To linearize E_T and E_r in Eqs. (13) and (14), we consider a basic temperature T_0* and its perturbation $T^{*\prime}$. The temperature T_0* is a function of the isobaric coordinate p* obtained from Eq. (7) when T_m is replaced by the constant T_{m0}. Likewise, $T^{*\prime}$ is obtained from Eq. (7), when T_m is replaced by $T_m' = T_m - T_{m0}$. Taking $T^* = T_0^* + T^{*\prime}$, expanding the function $E(T^*)$ in Taylor series and considering that $|T_m'|/T_0^* << 1$, we have:

$$E\left(T_0^* + T^{*\prime}\right) \cong E\left(T_0^*\right) + \left(\frac{dE}{dT^*}\right)_{T_0^*} T^{*\prime} \quad (15)$$

Then, the linearized form of equations (13) and (14) is:

$$E_T = F_{30} + F_{31} T_m' + F_{32} T_r' + \left(\alpha_2 + \alpha_3\right) I \quad (16)$$

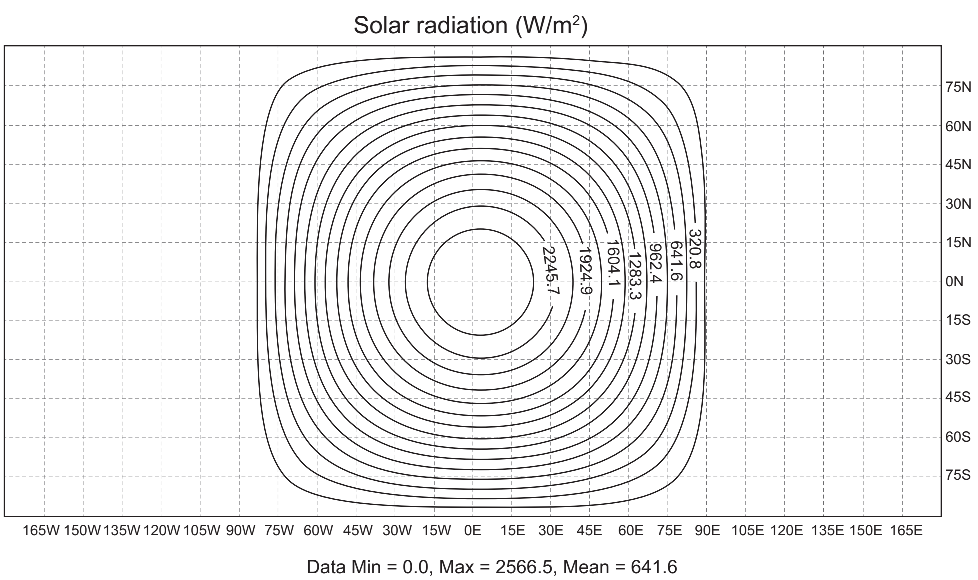

Fig. 2. Insolation or solar radiation at the planetary surface per unit area and time computed with Milanković's formula in the absence of an atmosphere.

$$E_r = F_{34} + F_{35}T'_m + F_{36}T'_r + \alpha_1 I \quad (17)$$

where $T'_r = T_r - T_{r0}$ is the perturbation of T_r and T_{r0} is a constant temperature. The constants F_n are:

$$\begin{aligned}
F_{30} &= -\sigma T^4_{C_{20}} - E\left(T_{S_0}\right) - \left[\sigma T^4_{C_{10}} - E\left(T_{C_{10}}\right)\right] + \sigma T^4_{r0} \\
F_{31} &= -4\sigma T^3_{C_{20}}\left(\frac{p}{p_m}\right)^{R\gamma} - \left(\frac{dE}{dT^*}\right)_{T_{S_0}}\left(\frac{p_s}{p_m}\right)^{R\gamma} - \left[4\sigma T^3_{C_{10}} - \left(\frac{dE}{dT^*}\right)_{T_{C_{10}}}\right]\left(\frac{p_c}{p_m}\right)^{R\gamma} \\
F_{32} &= 4\sigma T^3_{r0} \\
F_{34} &= -\sigma T^4_{r0} + E\left(T_{S_0}\right) + \left[\sigma T^4_{C_{10}} - E\left(T_{C_{10}}\right)\right] \\
F_{35} &= \left(\frac{dE}{dT^*}\right)_{T_{S_0}}\left(\frac{p_s}{p_m}\right)^{R\gamma} + \left[4\sigma T^3_{C_{10}} - \left(\frac{dE}{dT^*}\right)_{T_{C_{10}}}\right]\left(\frac{p_c}{p_m}\right)^{R\gamma} \\
F_{36} &= -F_{32}
\end{aligned} \quad (18)$$

The constant temperatures T_{S_0}, T_{C1_0}, and T_{C2_0} are obtained by replacing T_m with the constant T_{m0} in Eq (11). In the model $T_{r0} = T_{S_0} = 737$ K (464 ºC), which corresponds to the Venus average surface temperature (Vidmachenko, 2025). With T_{S_0}, the temperature T_{m0} can be found from Eq. (6) as follows:

$$T_{m_0} = T_{S_0}\left(\frac{p_m}{p_s}\right)^{R\gamma} \quad (19)$$

2.3 Thermal energy balance at the upper regolith layer.

The regolith upper layer temperature T_r is calculated from the equation of conservation of thermal energy. We assume that in this layer, the stored thermal energy can be neglected; therefore, the heat transfer by net radiation E_r, and the vertical turbulent sensible heat transport G_2 given to the atmosphere, are in balance with the heat G_1 transferred by thermal conductivity from the regolith upper layer to the underlying regolith layer. The equation is:

$$0 = E_r - G_2 + G_1 \quad (20)$$

Here, G_1 and G_2 are:

$$G_1 = \frac{k_v}{h_r}\left(T'_g - T'_r\right) \quad (21)$$

$$G_2 = k_2\left|V_s\right|\left[T'_r - T'_m\left(\frac{p_s}{p_m}\right)^{R\gamma}\right] \quad (22)$$

where k_v is the thermal conductivity coefficient; h_r is the thickness of the upper regolith layer; $T'_g = T_g - T_{g0}$ is the temperature perturbation of the subsurface with respect to the upper regolith layer T_g and T_{g0}. For the coefficient $k_2 = c\rho_{s0}\, c_p$, $c = 1.25 \times 10^{-3}$ is the constant coefficient of heat transfer; $\rho_{s_0} = \frac{p_s}{RT_{s_0}}$ is the atmospheric density at the surface considered as constant, and $|V_s|$ is the surface wind speed, which we assume constant with a value of 1.25 m s^{-1}, an intermediate value in the range of 2.0 m s^{-1}, and 0.5 m s^{-1} below 100 m, obtained from in-situ measurements (Lorenz, 2016). Working with Eqs. (17), (21) and (22) in Eq. (20), and using $T'_s = T'_m\left(\frac{p_s}{p_m}\right)^{R\gamma}$, we obtain the following equation for T'_r:

$$T'_r = F_{72} + F_{73}T'_m + F_{74}T'_g \quad (23)$$

Here:

$$\begin{aligned}
F_{71} &= -F_{36} + \frac{k_v}{h_r} + k_2\left|V_s\right| \\
F_{72} &= \frac{\left(F_{34} + \alpha_1 I\right)}{F_{71}} \\
F_{73} &= \frac{\left[F_{35} + k_2\left|V_s\right|\left(\frac{p_s}{p_m}\right)^{R\gamma}\right]}{F_{71}} \\
F_{74} &= \frac{k_v}{h_r F_{71}}
\end{aligned} \quad (24)$$

Substituting T'_r from (23) in (16) and (22), we found that the tropospheric heating in Eq. (8) can be expressed as:

$$E_T + G_2 = F_{81} + F_{80}T'_m + F_{79}T'_g \quad (25)$$

where:

$$\begin{aligned}
F_{78} &= F_{32} + k_2\left|V_s\right| \\
F_{79} &= F_{78}F_{74} \\
F_{80} &= F_{31} - k_2\left|V_s\right|\left(\frac{p_s}{p_m}\right)^{R\gamma} + F_{78}F_{73} \\
F_{81} &= F_{30} + \left(\propto_2 + \propto_3\right)I + F_{78}F_{72}
\end{aligned} \quad (26)$$

The temperature T'_g in Eqs. (23) and (25) is calculated using the equation of thermal conductivity in the regolith:

$$\rho_r c_r \frac{\partial T_r^{*\prime}}{\partial t} = k_v \frac{\partial^2 T_r^{*\prime}}{\partial z^2} \quad (27)$$

where ρ_r and c_r are the density and specific heat of the regolith and $T_r{*}'$ is the temperature of each regolith layer. In Eq. (27), the thermal conductivity coefficient is related to the thermal inertia I_T, by $I_T = \sqrt{\rho_r c_r k_v}$. For the surface layer, $T_r{*}' = T_r'$, and the subsurface layer (the second layer), $T_r{*}' = T_g'$.

2.4 The equations of motion

To compute the zonal and meridional wind components $U*$ and $V*$, respectively, where the zonal wind in Venus flow is positive in the westward to eastward direction, and the meridional wind is positive when flows from south towards the north pole, we will use the equations of horizontal motion, with $\zeta* = -ln(p*/p_s)$ as the vertical coordinate and assuming hydrostatic balance, where (as we mentioned in Eq. [5]), both $p*$ and p_s correspond to isobaric surfaces at levels z and $z = 0$, respectively. These equations are similar to those given by Saltzman (1978):

$$\frac{\partial U*}{\partial t} + \frac{U*}{a cos\varphi}\frac{\partial U*}{\partial \lambda} + \frac{V*}{a}\frac{\partial U*}{\partial \varphi} + \omega_\zeta^* \frac{\partial U*}{\partial \zeta*} - \left(f + \frac{U*}{a} tan\varphi\right) V* + \varepsilon* U* - \nu \nabla^2 U* = -\frac{1}{a cos\varphi}\frac{\partial \Phi_s^*}{\partial \lambda} \quad (28)$$

$$\frac{\partial V*}{\partial t} + \frac{U*}{a cos\varphi}\frac{\partial V*}{\partial \lambda} + \frac{V*}{a}\frac{\partial V*}{\partial \varphi} + \omega_\zeta^* \frac{\partial V*}{\partial \zeta*} + \left(f + \frac{U*}{a} tan\varphi\right) U* + \varepsilon* V* - \nu \nabla^2 V* = -\frac{1}{a}\frac{\partial \Phi_s^*}{\partial \varphi} \quad (29)$$

The vertical component of velocity $\omega_\zeta*$ is computed from the continuity equation:

$$\frac{\partial \omega_\zeta^*}{\partial \zeta*} + \omega_\zeta^* = \frac{1}{a cos\varphi}\left[\frac{\partial U*}{\partial \lambda} + \frac{\partial (V* cos\varphi)}{\partial \varphi}\right] \quad (30)$$

The vertical component of velocity $w*$ is positive when it flows from the surface to the top of the atmosphere (normal to the surface), where the vertical coordinate z is related to $\omega_\zeta*$ through the hydrostatic equation and the equation of state, resulting in the following approximation:

$$\omega_\zeta^* \cong \frac{\rho* g}{p*} w* = \frac{g}{RT*} w* \quad (31)$$

In Eqs. (28) and (29), the geopotential Φ_s* is given by Eq. (5); f is the Coriolis parameter; ν is the horizontal turbulent viscosity coefficient, and $\varepsilon*$ is the Rayleigh drag coefficient. Furthermore, following the idea of the Rayleigh friction model (Stevens et al., 2002), the zonal and meridional components of the vertical gradient of turbulent stress can be expressed for the troposphere as $-\varepsilon* U*$ and $-\varepsilon* V*$, respectively. These terms have the effect of slowing down the horizontal motion of the atmosphere and are thought to originate in the process of thermal convection, vertical turbulence (between 40 and 60 km), weak random eddies in the planetary boundary layer (PBL), and gravity waves excited by mountains (Gierasch, 1975; Schubert et al., 1980; Lefèvre, 2022). We further assume that the efficiency with which vertical turbulence slows horizontal motion depends on atmospheric density. In this way, we propose that:

$$\varepsilon* = \varepsilon_s\left(\frac{\rho*}{\rho_s}\right) = \varepsilon_s\left(\frac{p*}{p_s}\right)^{1-R\gamma} \quad (32)$$

where we used the ideal gas equation, and ε_s and ρ_s are the values of $\varepsilon*$ and $\rho*$ at the surface. Stevens et al. (2002) use $\varepsilon_s = 2.2 \times 10^{-5}$ s^{-1}, and we adjusted this value empirically from the experiments to $\varepsilon_s = 1.5 \times 10^{-5}$ s^{-1}.

When the meridional equatorward component of the centrifugal force is in balance with the meridional poleward component of the force due to the geopotential gradient, then the circulation of the atmosphere is in cyclostrophic balance. These components are part of the equation of motion (Eq. [29]), so that the cyclostrophic balance can be expressed as:

$$U^{*2} tan\varphi = -\frac{\partial \Phi_s^*}{\partial \varphi} \quad (33)$$

In spherical coordinates, the Laplacian in Eqs. (4), (28), and (29) for any continuous scalar function and with continuous derivatives is given by:

$$\nabla^2 \psi = \frac{1}{a cos\varphi}\left[\frac{1}{a cos\varphi}\frac{\partial^2 \psi}{\partial \lambda^2} + \frac{1}{a}\frac{\partial}{\partial \varphi}\left(cos\varphi \frac{\partial \psi}{\partial \varphi}\right)\right] \quad (34)$$

2.5 Numerical solutions of the equations

To numerically solve Eqs. (28) and (29), we used the semi-implicit method, approximating the time derivatives by the corresponding finite differences: $\frac{(U^*-U_p^*)}{\Delta t}$ and $\frac{(V^*-V_p^*)}{\Delta t}$, where Δt is the 1 h time step, and U_p* and V_p* are the corresponding U* and V* values in the previous time step and using U_p* and V_p* instead of U* and V* in the momentum advection and convection terms and in the $-\frac{U^*V^*}{a}\,tan\varphi$ and $-\frac{U^*U^*}{a}\,tan\varphi$ terms of Eqs. (28) and (29), respectively; in this way, using Eq. (34), we have a set of coupled differential equations given by:

$$\nu\left(\frac{1}{a^2cos\varphi^2}\frac{\partial^2U^*}{\partial\lambda^2}+\frac{1}{a^2}\frac{\partial^2U^*}{\partial\varphi^2}\right)-\frac{\nu\, tan\varphi}{a^2}\frac{\partial U^*}{\partial\varphi}-\frac{U_p^*}{acos\varphi}\frac{\partial U^*}{\partial\lambda}-\frac{V_p^*}{a}\frac{\partial U^*}{\partial\varphi}-\omega_{\zeta p}^*\frac{\partial U_p^*}{\partial\zeta^*}+\left(f+\frac{U_p^*}{a}tan\varphi\right)V_p^*-\left(\varepsilon^*+\frac{1}{\Delta t}\right)U^*+\frac{1}{\Delta t}U_p^*-\frac{1}{acos\varphi}\frac{\partial\Phi_s^*}{\partial\lambda}=0 \tag{35}$$

$$\nu\left(\frac{1}{a^2cos\varphi^2}\frac{\partial^2V^*}{\partial\lambda^2}+\frac{1}{a^2}\frac{\partial^2V^*}{\partial\varphi^2}\right)-\frac{\nu\, tan\varphi}{a^2}\frac{\partial V^*}{\partial\varphi}-\frac{U_p^*}{acos\varphi}\frac{\partial V^*}{\partial\lambda}-\frac{V_p^*}{a}\frac{\partial V^*}{\partial\varphi}-\omega_{\zeta p}^*\frac{\partial V_p^*}{\partial\zeta^*}-\left(f+\frac{U_p^*}{a}tan\varphi\right)U_p^*-\left(\varepsilon^*+\frac{1}{\Delta t}\right)V^*+\frac{1}{\Delta t}V_p^*-\frac{1}{a}\frac{\partial\Phi_s^*}{\partial\varphi}=0 \tag{36}$$

where $\omega^*_{\zeta p}$ is the corresponding value of ω^*_ζ in the previous time step and is computed from the continuity Eq. (30), using U_p* and V_p* instead of U* and V*, respectively.

Eqs. (35) and (36) can be written as a single equation as follows:

$$\nu\left(\frac{1}{a^2cos\varphi^2}\frac{\partial^2\psi}{\partial\lambda^2}+\frac{1}{a^2}\frac{\partial^2\psi}{\partial\varphi^2}\right)+\frac{F_{84}}{acos\phi}\frac{\partial\psi}{\partial\lambda}+\frac{F_{85}}{a}\frac{\partial\psi}{\partial\varphi}+F_{89}\psi+F_{90}=0 \tag{37}$$

For the case $\psi = U$* we have:

$$F_{84}=-U_p^*$$

$$F_{85}=-\frac{\nu tan\varphi}{a}-V_p^*$$

$$F_{89}=-\frac{1}{\Delta t}-\varepsilon^*$$

$$F_{90}=\frac{1}{\Delta t}U_p^*-\omega_{\zeta p}^*\frac{\partial U_p^*}{\partial\zeta^*}+\left(f+\frac{U_p^*}{a}tan\varphi\right)V_p^*-\frac{1}{acos\varphi}\frac{\partial\Phi_s^*}{\partial\lambda}$$

For the case $\psi = V$*, F_{84}, F_{85} and F_{89} do not change, while:

$$F_{90}=\frac{1}{\Delta t}V_p^*-\omega_{\zeta p}^*\frac{\partial V_p^*}{\partial\zeta^*}-\left(f+\frac{U_p^*}{a}tan\varphi\right)U_p^*-\frac{1}{a}\frac{\partial\Phi_s^*}{\partial\varphi}$$

Substituting the tropospheric heating $E_T + G_2$ from Eq. (25) in the thermodynamic Eq. (8) and using the approximation $\frac{\partial T'_m}{\partial t}\cong\frac{(T'_m-T'_{mp})}{\Delta t_0}$, where T'_{mp} is the temperature T'_m in the previous time step Δt_0, which is one terrestrial day, we found a similar equation to Eq. (37), where $\psi = T'_m$ and where the coefficient is replaced by the Austausch coefficient K and:

$$F_{84}=0$$

$$F_{85}=-\frac{K\,tan\varphi}{a}$$

$$F_{89}=-\frac{1}{\Delta t_0}+\frac{F_{80}}{F_2}$$

$$F_{90}=\frac{T'_{mp}}{\Delta t_0}+\frac{F_{81}}{F_2}+\frac{F_{79}}{F_2}T'_g$$

Our method of obtaining the superrotation of the Venusian atmosphere is based on a simplified realistic thermodynamic model, from which we can obtain the geopotential given by Eq. (5) in terms of the atmospheric surface temperature T_s, which can be expressed in terms of T_m, using the first equality in Eq. (11). Temperature T_m is computed from the thermodynamic Eq. (8), where the advection and convection of thermal energy have been neglected; in this way, the complex coupling between the thermodynamic equation and the dynamic equations is excluded from the problem, and consequently, the dynamics are subordinated to the thermodynamic state of the atmosphere.

Eq. (37), for the cases in which corresponds to the wind components U^* and V^* or to the temperature $T'm$, is integrated using finite differences centered for the space derivatives in a latitude φ between –89.5º and 89.5º, and a longitude λ between 0.5º and 359.5º; in radians: $\varphi_j = \frac{(j-90.5)\pi}{180}$; $j = 1,2,\ldots,180$, and $\lambda_i = \frac{2(i-0.5)\pi}{360}$; $i = 1,2,\ldots,360$,, then $\Delta\varphi = \frac{\pi}{180}$ and $\Delta\lambda = \frac{2\pi}{360}$ are the latitude and longitude intervals, respectively. Eq. (37) can be a second-order linear elliptic differential equation depending either on the turbulent viscosity coefficient or on the Austausch coefficient K. Assuming this is the case, the equations can be solved using the Liebmann relaxation method (Thompson, 1961).

The model equations given by Eq. (37) are not applied at the poles, since, in spherical coordinates, these points can result in singularities. In this way, to carry out the spatial derivatives of temperature and velocities with respect to latitude on the borders, defined by the latitude circles close to the poles ($\{j = 1;\ i = 1,2,\ldots,360\}$ for the south pole and $\{j = 180;\ i = 1,2,\ldots,360\}$) for the north pole, we assign for the grid point at each pole, the average temperature over the corresponding border, while U^*, V^* and $\omega^*_{\zeta p}$ are taken as zero at the pole grid points.

Therefore, the derivatives with respect to φ at the boundaries are: $\left(\frac{\partial\psi}{\partial\varphi}\right)_{i,1} = 2(\psi_{i,2} - \psi_{sp})\ /3\Delta\varphi$ for the southern border and $\left(\frac{\partial\psi}{\partial\varphi}\right)_{i,180} = 2(\psi_{np} - \psi_{i,179})\ /3\Delta\varphi$ for the northern border, where ψ_{sp} and ψ_{np} is the value of at the south pole and north pole, respectively.

The thermodynamic model equations are the thermodynamic equation, Eq. (8) for the atmosphere and Eq. (20) for the surface, the thermal conductivity Eq. (27), the movement, Eqs. (28) and (29), and the continuity equation, Eq. (30).

To integrate the thermal conductivity equation, Eq. (27), the regolith is divided into 24 layers, including the surface layer. The thickness of each layer varies and is given $\Delta z = h_r\ exp[0.1(n-1)]$, with $n = 1,2,\ldots,24$; then for $n = 1$, $\Delta z = h_r = 0.20$m and for $n = 24$, $\Delta z = 1.99$ m, resulting in a thickness of 19.1 m for the complete regolith layer. We employ centered differences using 1 h time steps for spatial and temporal derivatives. The border conditions are $T_r{*}' = T_r'$ for the upper layer and $\frac{\partial T_r^{*\prime}}{\partial z} = 0$ for the deepest layer.

The velocity is computed in 24 levels from the surface $\zeta^* = 0$ to the top of the troposphere $\zeta^* = -\ln(p_H/p_s) = 7.846$), these levels are separated from each other by $\Delta\zeta = -\ln(p_H/p_s)\ /\ 24 = 0.327$. In this way, using finite differences centered on the vertical, the continuity Eq. (30) can be expressed as:

$$\left(\omega^*_{\zeta_p}\right)_{k+1} = \frac{(1-\Delta\zeta)}{(1+\Delta\zeta)}\left(\omega^*_{\zeta_p}\right)_{k-1} + \frac{2\,\Delta\zeta}{(1+\Delta\zeta)}\frac{1}{a\cos\varphi}\left[\frac{\partial U_p^*}{\partial\lambda} + \frac{\partial(V_p^*\cos\varphi)}{\partial\varphi}\right]_k \tag{38}$$

where $k = 1,2,3,\ldots,24$ and where we have used the approximation $(\omega^*_{\zeta p})_k = [(\omega^*_{\zeta p})_{k+1} + (\omega^*_{\zeta p})_{k-1}]\ /\ 2$, assuming that on the surface $\omega^*_{\zeta p} = 0$.

For the vertical momentum transport terms $\omega^*_{\zeta_p}\frac{\partial U_p^*}{\partial\zeta^*}$ and $\omega^*_{\zeta_p}\frac{\partial V_p^*}{\partial\zeta^*}$ in Eqs. (35) and (36), respectively, we also use centered finite differences, assuming that at $\zeta^* = 0$, $U_p^* = 0$ and $V_p^* = 0$, which is in some agreement with the observations that indicate that for altitudes less than 7 km, the magnitude of the wind is usually ~1 m s^{-1}, comparable to the experimental noise level of ± 1 m s^{-1} (Schubert et al., 1980). Takagi and Matsuda (2007) found that the downward transport of zonal momentum from the cloud layer to the lowest layer of their model, associated with the semidiurnal thermal tide, induces a near-surface mean zonal flow opposite the rotation of Venus so that surface friction acts on this counterflow. This may be the possible cause of a slow westerly zonal wind near the surface. According to Moroz and Zasova (1997), the zonal wind profiles presented in the VIRA program suggest that the zonal wind reaches a maximum at the top of the clouds; therefore, we assume that its derivative with respect to height is zero at this level. This same boundary condition is assumed for the meridional component. Then, at the top of the troposphere, we assume that $\frac{\partial U_p^*}{\partial\zeta^*}$ and $\frac{\partial V_p^*}{\partial\zeta^*}$ are zero.

The vertical velocity w^* in z coordinates can be determined in terms of the vertical velocity $\omega_\zeta{}^*$ using the hydrostatic equilibrium equation and the equation of state and Eq. (31).

The initial conditions for the temperature perturbations are $T'_{mp} = 0$, $T^{*\prime}_{rp} = 0$ for each regolith layer, $U_p^* = V_p^* = 0$ and $\omega^*_{\zeta p} = 0$ for the velocities at each ζ^* level. First, we integrate the thermal conductivity Eq. (27) using 24-time steps of 1 h to complete one terrestrial day; the temperature T'_g obtained in the last time step is used to integrate the thermodynamic Eq. (8), where we use time steps of one Earth day. The computed tropospheric temperature T'_m is expressed in terms of T'_s using the first equation in Eq. (11) and with Eq. (5) we calculate the potential Φ_s*; finally, with Eqs. (35) and (36) and the continuity Eq. (38), we calculate the velocity components U^* V^* and ω_ζ^*, using 24-time steps of 1 h. With T'_m and T'_g we calculate T'_r using Eq. (21). The next steps are similar, using T'_m, U^*, V^* and T'_g computed in the previous time steps as initial conditions in the prognostic equations. The model is integrated for 300 Venus days until the tropospheric temperature, wind, and tropospheric angular momentum are stabilized; this is achieved after ~86 Venusian days (~10 062 Earth days).

3. Data

The atmospheric layer emission spectrum is found from the spectral calculator E-TRANS using the database HITRAN (Rothman et al, 2009), resulting in an emission spectrum close to that of a black body. The surface regolith and the cloud cover are considered black bodies themselves.

Meridional profiles of the zonal wind and the mean north-south wind (m s^{-1}) were obtained from cloud tracking measured at UV wavelengths at an altitude between 65 and 70 km of the Mariner 10 missions, 1974; Pioneer-Venus, 1980, 1982; Galileo, 1990; Venus Express VIRTIS, 2006-2012 and Venus Express VMC, 2006-2012 in the daytime (Sánchez-Lavega et al., 2017).

We also used data from the Venera vertical profiles 8, 9, 10, and 12 and Pioneer-Venus reported by Schubert et al. (1980).

4. Results and discussion

The experiments that comprise this work are three: the baseline experiment (BL experiment), which includes all terms in the equations; the experiment in which the zonal gradient of the geopotential is set to zero (ZGZ experiment); and the experiment in which vertical momentum transport is set to zero (VMTZ experiment).

The surface temperature (K) of the Venusian atmosphere calculated by the model at the beginning of the 300th Venusian solar day (that is, 34 984 Earth days), when the maximum insolation is located at 0º E longitude (see Fig. 2), is shown in Figure 3. The maximum surface heating occurs at the equator, between 75º and 60º W, and advances behind the

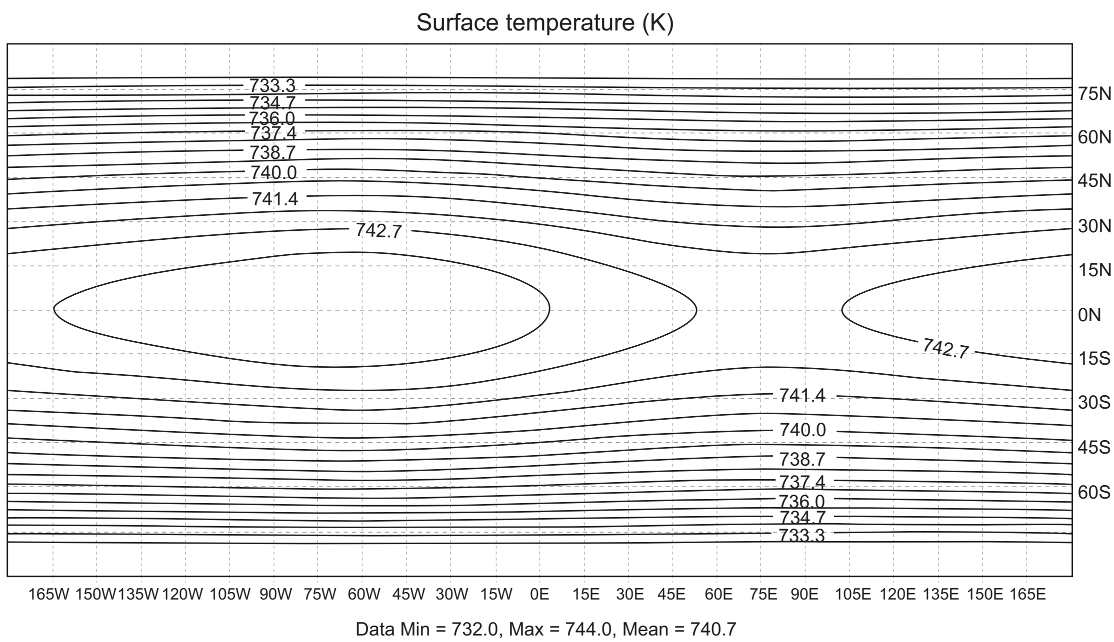

Fig. 3. The Venusian atmosphere's surface temperature (K) was computed at the beginning of the 300th Venusian day (Earth day 34 984).

maximum insolation. Due to the meridional gradient of insolation, the temperature difference between the equator and the poles is ~12.0 K. The maximum surface temperature on the equator is reached just before sunset, while the minimum is reached shortly after sunrise. This thermal contrast of 12.0 K between the equator and the pole is considerably greater than that simulated by a GCM, shown in Figure 1a of Takagi et al. (2018), which is in the order of 1 to 4 K. The thermal contrast between the equator and the pole at the clouds upper level (~70 km) can be determined by our model applying Eq. (6) at this level, when $p^* = p_H = 3.6 \times 10^3$ Pa, where the temperature $\langle T^* \rangle = T_{c2}$. Then, T_{c2} = 204.1 K T at the equator, and T_{c2} = 200.6 K at the pole, resulting in the thermal contrast of 3.5 K at this level. This shows an agreement with Figure 1 from Takagi et al. (2018), where the thermal contrast ranges from 0 to 5 K at the same level. Along the equator, the difference between the maximum and minimum temperatures, which is reached at sunrise, is only ~2.9 K. The lag between insolation and surface temperature may be due to the storage of thermal energy in the massive atmosphere of Venus and the thermal inertia of its regolith, which is 10 times greater than that of the Martian regolith (Mendonça and Buchhave, 2020; Mendoza et al., 2021). The high Venus surface atmospheric pressure broadens the CO_2 absorption bands in the infrared spectrum, particularly the 15-µm band, to the point where the atmospheric layer emits and absorbs infrared radiation almost like a black body, causing a powerful greenhouse effect that elevates the surface temperature of the atmosphere up to ~744 K (471 ºC) on the equator (Fig. 3).

For the BL experiment, the computed time series of the surface temperature (K) (in red) and the zonal and meridional components of the wind (m s^{-1}) at ~68.5 km altitude (in blue and purple, respectively) are shown in Figure 4. The model runs for 300 Venusian days (35 100 Earth days) to ensure that temperature and wind reach a stable condition, which begins to occur after ~86 Venusian days (10 062 Earth days). The temperature (Fig. 4a) corresponds to the average in the tropical region from 20.5º S to 20.5º N and 173.5 to 185.5º E. In comparison, the wind components (Fig. 4b) correspond to the north latitude region between 24.5 and 73.5º N and between 173.5 and 185.5º E. The last seven Venus days (819 Earth days) of this run are also shown for the temperature and wind components (Fig. 4c). The thermal and dynamic oscillation period is 117 Earth days, which is one Venusian solar day. The tropical temperature oscillation has an amplitude of ~1.4 K, that is, between 743.8 K just before sunset (see Figs. 2 and 3) and 742.4 K at sunrise, while the zonal and meridional wind components oscillate between –80.2 and –102.45 m s^{-1} (~22 m s^{-1}), and 13.5 and –10.5 m s^{-1} (~24 m s^{-1}), respectively. The temperature and zonal wind are out of phase by ~48 Earth days, while the temperature and the meridional wind by ~22 days.

We consider that the radiation balance E_T in the troposphere of Venus, given by Eq. (13), which includes the radiation balance of the cloud layer, and the radiation balance E_r at the regolith surface, given by Eq. (14), are appropriate since when used in the thermodynamic Eqs. (8) and (20), respectively, they give as a solution a global mean atmospheric temperature at the surface level of 740.7 K (see Fig. 3) with certain agreement with observations (Lorenz et al., 2018). In addition, the oscillations indicate that said temperature remains stable during the 300 Venusian days of the model run (Fig. 4).

If we assume the atmosphere of Venus rotating as a solid body equal to the rotation of the planet, so that its zonal velocity turns out to be equal to a Ωcosφ, then its total angular momentum can be calculated, integrating the density of the angular momentum ρ^* (aΩcosφ)acosφ over the entire volume of the atmosphere; the result is $(8/3\ \pi a^4\ \Omega p_s)/g = 3.47 \times 10^{27}\ kgm^2\ s^{-1}$. On the other hand, the relative angular momentum of the atmosphere M_r, associated with the zonal wind U^*, is calculated by integrating the angular momentum density $\rho^*\ U^*\ acos\varphi$ over the entire volume of the atmosphere. According to Golitsyn (1984), the result of this integral is in the range of (3 to 4)×10^{28} kg m^2 s^{-1}. Figure 5 shows the relative angular momentum of the troposphere calculated by our model, whose value 3.2 × 10^{28} kg m^2 s^{-1} is reached approximately after Venusian day 60. This computed value is within the range of values given by Golitsyn (1984).

The computed components of the zonal and meridional wind and vertical velocity, as a function of latitude and altitude, are shown in Figure 6. These results show a prograde zonal wind (zonal winds moving in the same direction of the planet's rotation)

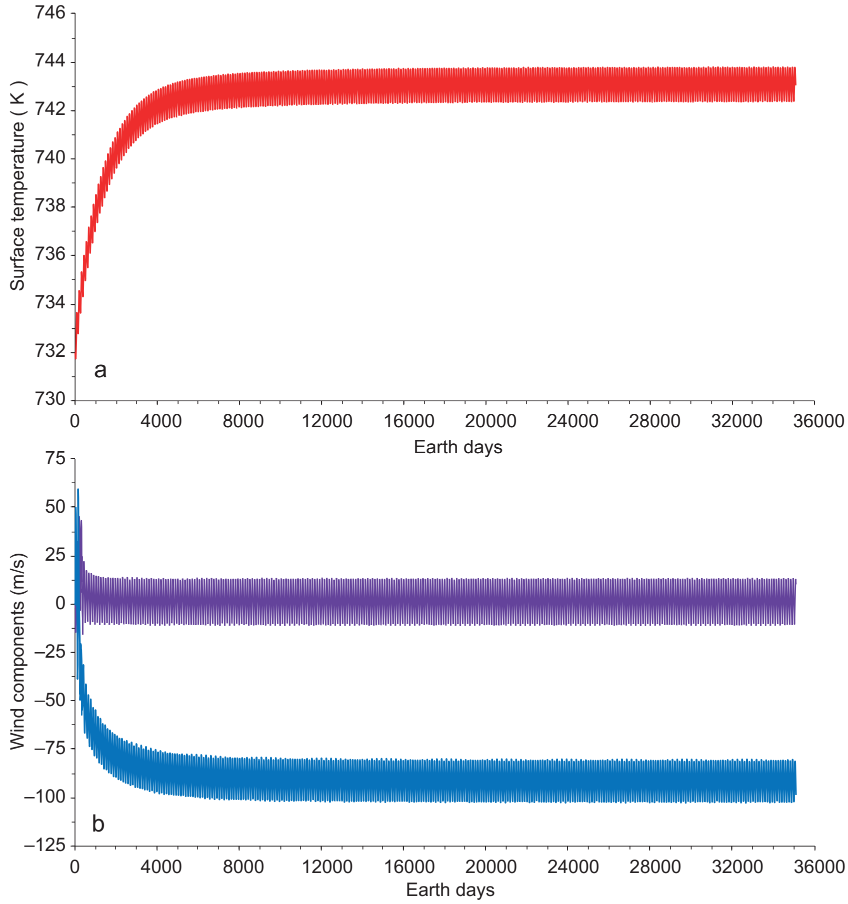

Fig. 4. Modeled time series for 300 Venus solar days. (a) Computed average surface temperature in the tropical region between 20.5º S and 20.5º N, and 173.5 to 185.5º E; (b) computed average zonal and meridional wind components at ~68.5 km of altitude (blue and purple curves, respectively) in the northern region between 24.5 to 73.5º N, and 173.5 to 185.5º E; (c) the last seven Venus days of these series for the temperature and the wind components.

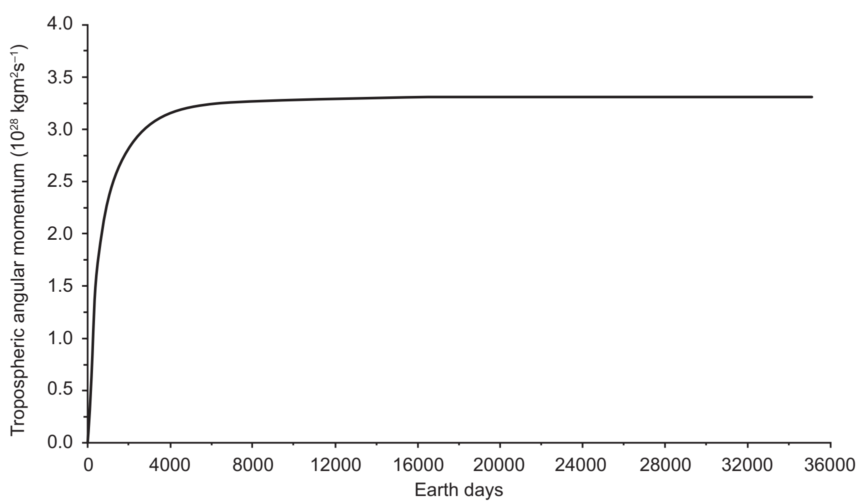

Fig. 5. Relative angular momentum (10^{28} kg m^2 s^{-1}) of the troposphere associated with the zonal wind calculated by the model.

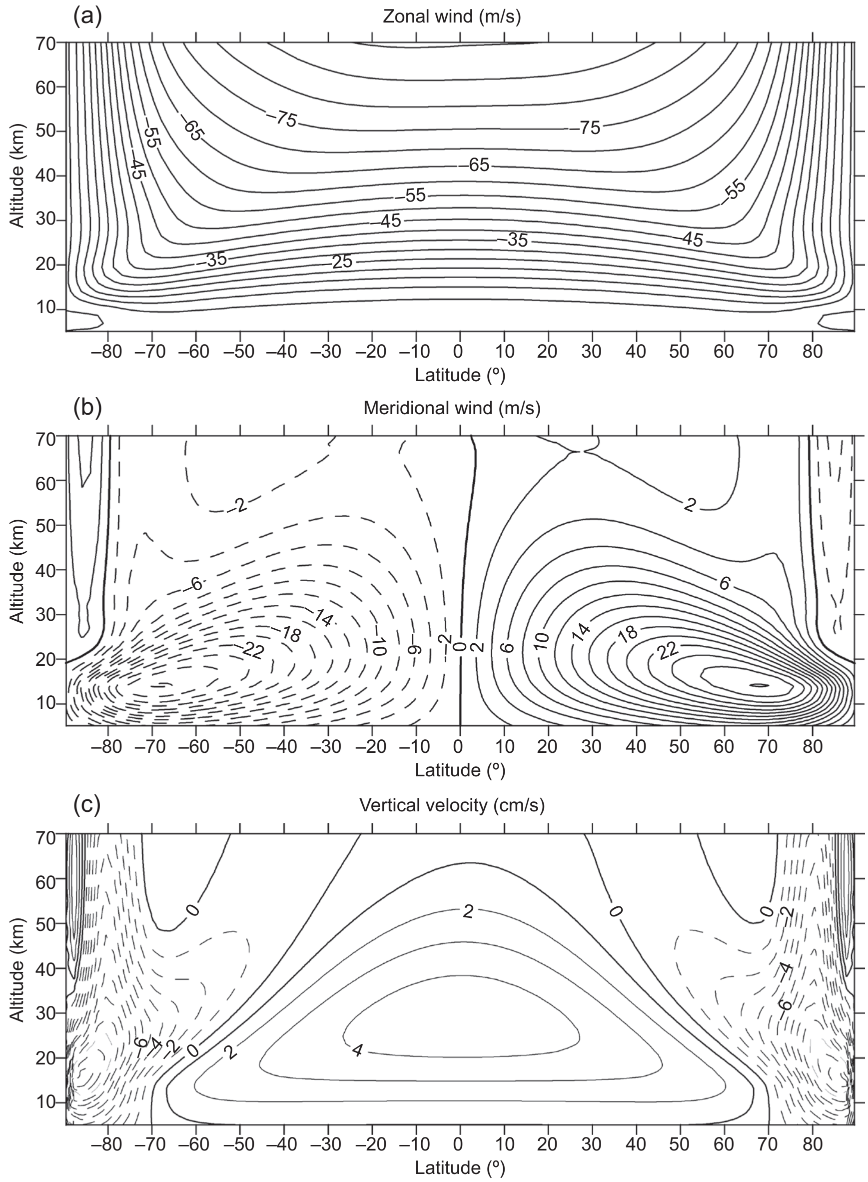

Fig. 6. Computed components of the (a) zonal, (b) meridional, and (c) vertical velocity as a function of latitude and altitude. These velocity components correspond to the average of the last Venusian day. The vertical velocity is computed using Eq. (31).

throughout the troposphere (Fig. 6a) that increases with altitude and towards the equator until reaching wind speeds greater than 75 m s^{-1} above 50 km altitude. Near the top of the troposphere (~70 km), a prograde tropical jet (between –20º and 20º latitude) is established with a speed of ~90 m s^{-1}. When comparing the zonal component of the wind simulated by our model (Fig. 6a) with the intercomparison of the eight GCMs in Figure 8.2 of Lebonnois et al. (2013), we find that these models exhibit a significantly different wind pattern compared with the simulation produced by our model, for example, the UCLA high resolution finite volume model simulates only a 50 m s^{-1} equatorial jet at an altitude of ~70 km (~3.6×10^3 Pa). As the equatorial air rises (Fig. 6c), it moves towards the poles (Fig. 6b), where it descends (Fig. 6c) after

±20° latitude, suggesting the establishment of a direct thermal circulation (DTC).

In the polar regions (between 60 and 70º latitude) at an approximate altitude of 15 km, strong winds develop towards the poles that exceed 28 m s^{-1}. This DTC, which exceeds 10 m s^{-1} below ~40 km altitude (Fig. 6b), suggests two large asymmetric Hadley cells in both hemispheres whose thickness is greater near the equator, where the air rises, reducing towards the poles, where the air descends. However, the meridional circulation does not show an overturning branch (Fig. 6b), which may be due to the simplification of our model in comparison with the GCMs, which show a more complex meridional circulation with several superposed cells, when these models incorporate a realistic radiative transfer and the topography (Lebonnois et al., 2010).

Gierasch et al. (1997) present a vertical profile of *w**, obtained with a simplified model that predicts vertical velocities in the Hadley cells of the order of 10 m s^{-1}. According to Figure 6c, our results show lower values: near the equator, the upward flow, between 35 and 70 km altitude, is ~2 cm s^{-1}; in mid-latitudes (± 45º) it is ~1.0 cm s^{-1}, and close to the poles (± 80º), where there is air subsidence, it is between ~–6.0 cm s^{-1} at ~70 km altitude, and ~–1.0 cm s^{-1} near the surface.

A clear prograde zonal flow at cloud level (68.5 km), whose velocity increases from the poles toward the equator, is shown in Figure 7a. During the night (see Fig. 2), two large polar jets are established in both hemispheres (~30 N and ~30 S), heading towards the dayside with wind speeds closer to –100 m s^{-1} heading towards the equator. These jets are associated with the air descent shown in Figure 7c.

The model result has a significant discrepancy with observations and high-resolution modeling (e.g., Fujisawa et al., 2022) regarding meridional circulation at the cloud-top level. While previous studies indicate a daytime poleward flow, our scheme produces a flow from the poles to the equator with speeds exceeding 10 m s^{-1}.

This fundamental difference can be attributed to a key simplification in the thermodynamic approach: integrating the thermal energy equation for the entire tropospheric column (Eq. [1]) using a constant lapse rate, rather than performing a level-by-level radiative heating calculation. This approximation, combined with the troposphere's high thermal inertia, introduces a lag between the instantaneous peak insolation and the resulting peak surface temperature. Since the vertical thermal profile is constant, this surface temperature pattern and its lag are projected to remain unchanged at all levels, including the cloud top (approximately 70 km).

Consequently, the region of maximum atmospheric heating in the model shifts toward the night side. Because the geopotential field—and thus the driving force for the meridional wind—is derived directly from this temperature, the resulting cloud-level circulation is reversed: the equator-to-poles flow occurs at night, and the poles-to-equator flow occurs during the day. This outcome contrasts with mechanisms in which cloud-level heating is predominantly direct and diurnal, generating a circulatory response in phase with the Sun.

It is important to mention that the surface temperature field (Fig. 3) and the planetary waves associated with the velocity components (Fig. 7) move in the same direction as the insolation (Fig. 2), that is, from west to east; however, the direction of the zonal wind associated with the superrotation is in the same direction in which the planet rotates; that is, a prograde zonal wind.

It is interesting to determine the relative importance of the zonal and meridional gradients of the geopotential contribution to the superrotation of the Venusian atmosphere. In this way, Figure 8a, b obtained in the ZGZ experiment (zonal gradient of the geopotential equal to zero), shows that the meridional gradient of the geopotential due to the meridional insolation gradient is sufficient to generate superrotation of the Venusian atmosphere in the dynamic equations.

Figure 9, obtained in the BL experiment, shows that in the high-latitude jet region (60º N and 60º S), the circulation is markedly zonal; however, at dawn, there is a meridional movement towards the equator in both hemispheres contributing to the equatorial jet; at sunset (~75º W in Figure 2) the meridional movement changes direction, now heading towards the poles, increasing the speed of the wind by conservation of angular momentum. An asymmetric vortex is established at each pole (b) and (c), with its maximum velocity forming part of the high-latitude jet.

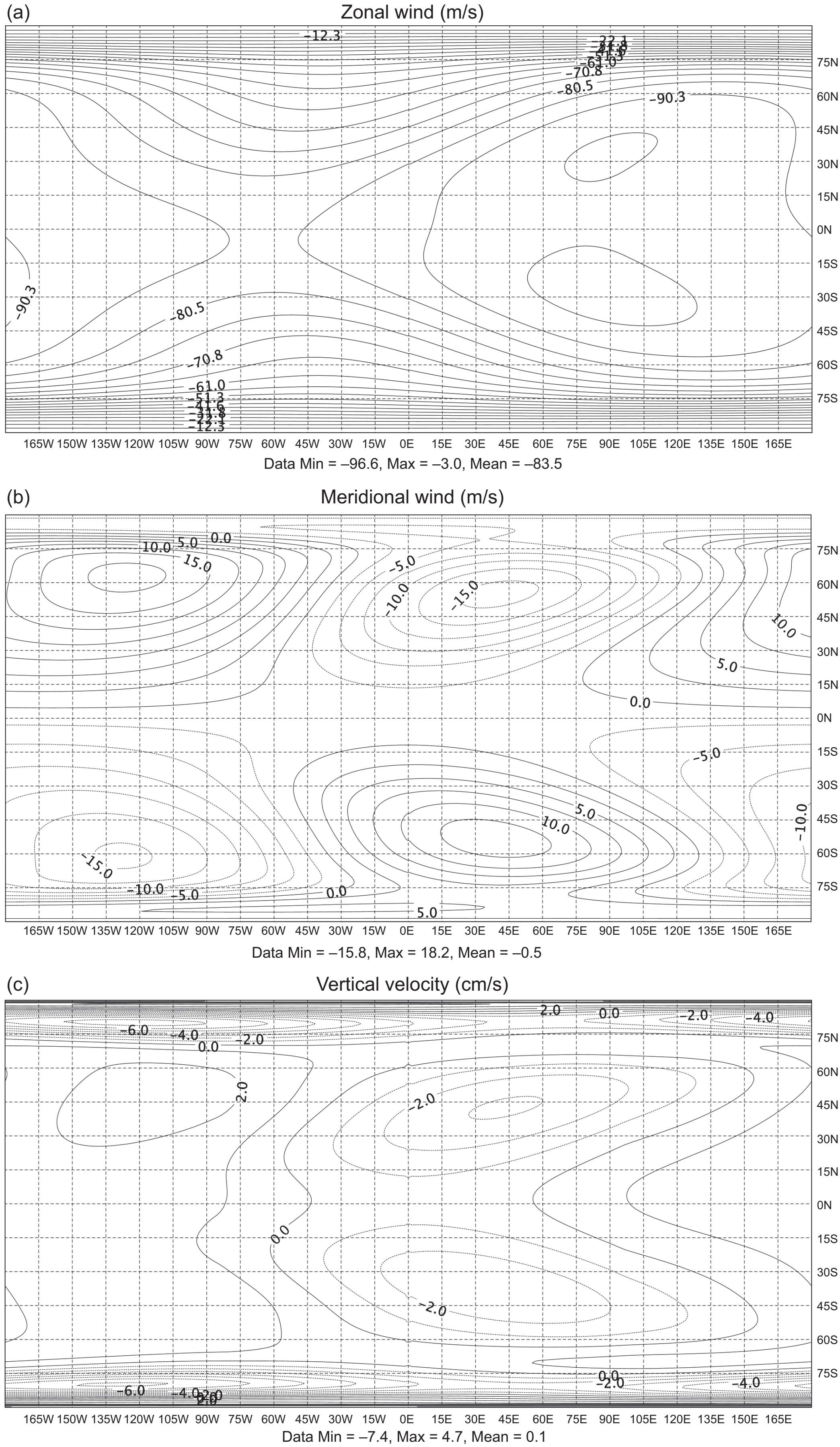

Fig. 7. Velocity components are now shown as a function of latitude and longitude at an altitude of ~68.5 km (5.0×10^3 Pa). These components correspond to those calculated at the beginning of the last Venusian day (Earth day 48 358): (a) zonal wind (m s^{-1}); (b) meridional wind (m s^{-1}); and (c) vertical velocity (cm s^{-1}).

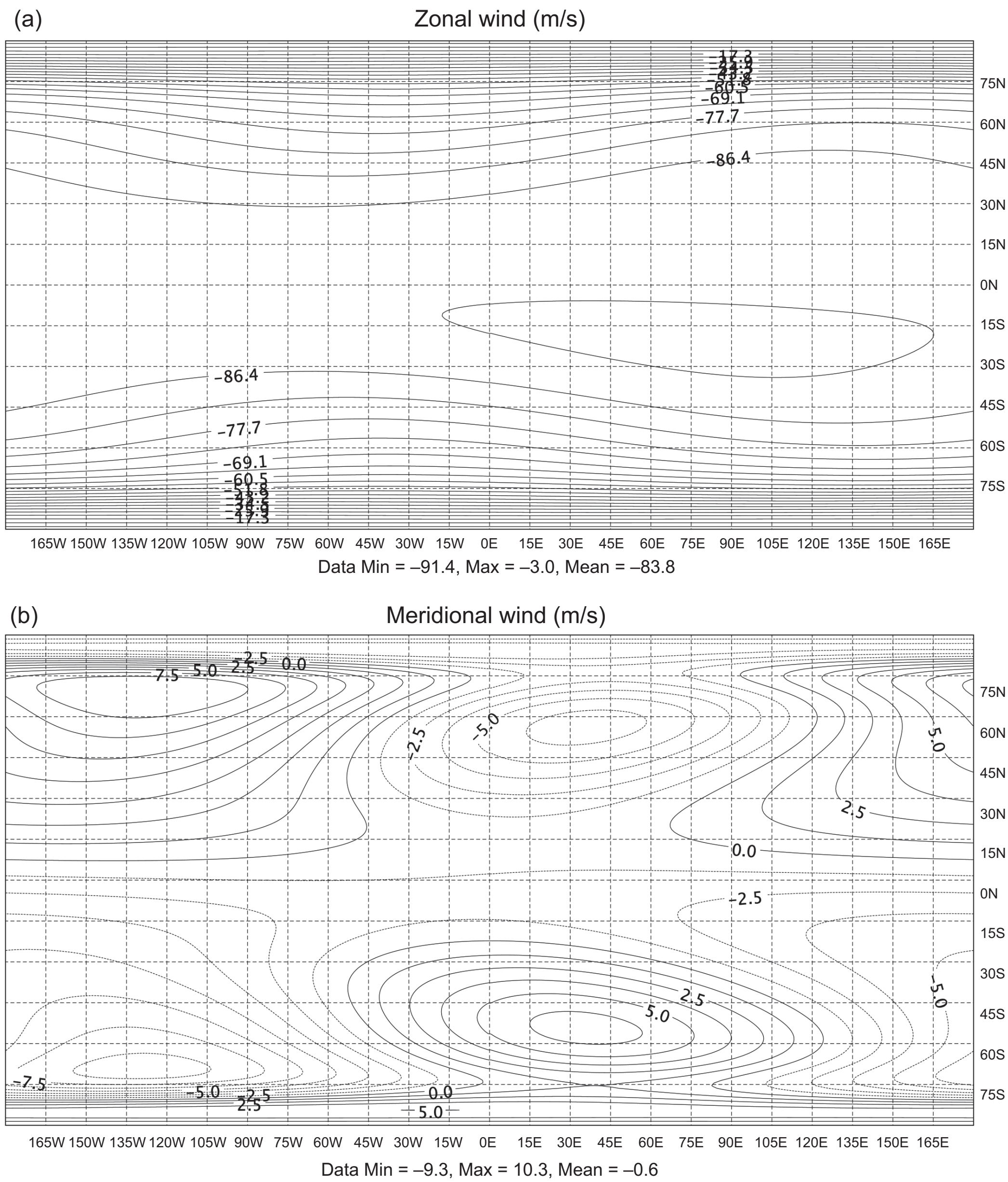

Fig. 8. (a) Zonal and (b) meridional components of the wind (m s^{-1}) at an altitude of ~68.5 km, where we have neglected the zonal gradient of the geopotential; that is, we assumed that $\partial\Phi_s{}^*/\partial\lambda$ = 0 in Eq. (28).

5. Comparison with observations in the BL experiment

Figure 10 shows the meridional profiles of the zonal wind (m s^{-1}) obtained from cloud tracking measured at UV wavelengths at an altitude between 65 and 70 km. The wind profile curves are not shown here but are within the gray area of this figure and are averages from the Mariner 10 missions, 1974; Pioneer-Venus, 1980, 1982; Galileo, 1990; Venus Express VIRTIS, 2006-2012, and Venus Express VMC, 2006-2012 in the daytime. Figure 2 of Sánchez-Lavega et al. (2017) shows these profiles. The black solid curve corresponds to the average made during the hours of sunshine and is calculated

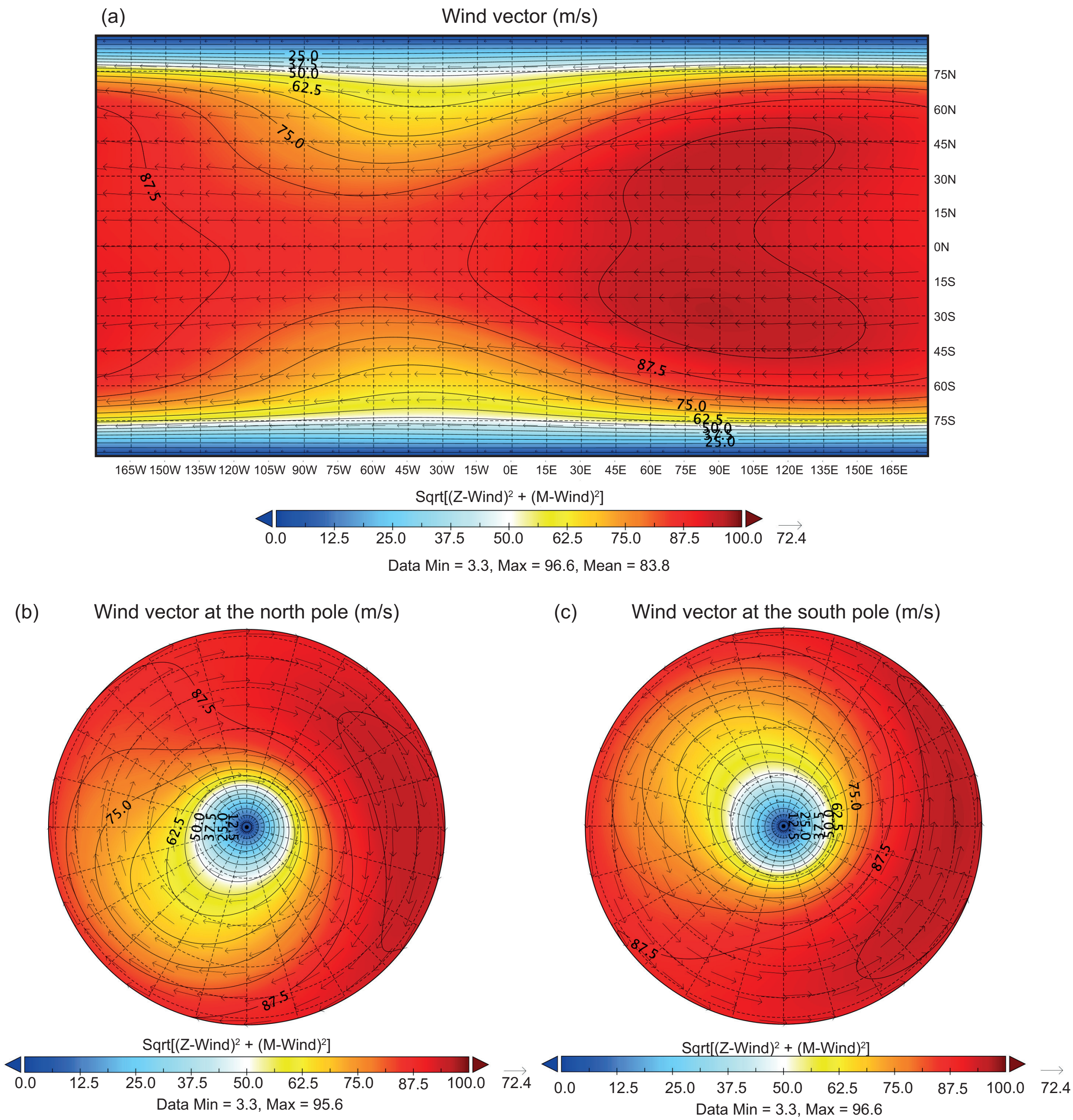

Fig. 9. Wind vector field computed at ~68.5 km altitude. (a) The field is shown in the equirectangular projection, and (b) and (c) in the orthographic Northern and Southern Hemisphere projections, respectively. Wind speed is represented in colors and its value is given in the color bar.

using the motion equations (Eqs. [35] and [36]) at the ~68.5 km level. The dotted curve is calculated using cyclostrophic equilibrium (Eq. [33]) at the same level, with the zonally averaged geopotential gradient and the square root multiplied by –1. At an altitude of 68.5 km, we find that the computed meridional profile lies within the range of observed values and is close to the meridional wind profile

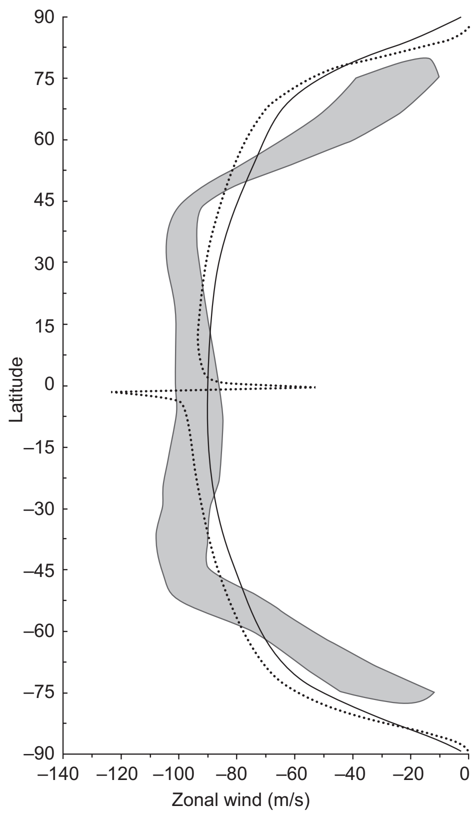

Fig. 10. Meridional profiles of zonal wind (m s^{-1}) obtained from cloud tracking at UV wavelengths during daytime in the altitude range between 65 and 70 km. The profiles, which are not shown here, are present within the gray area. Our model calculates the black solid curve and the dotted curve at ~68.5 km. The solid curve is calculated with the equations of motion (Eqs. [35] and [36]) and corresponds to the average made during the hours of sunshine; the dotted curve is calculated with the cyclostrophic balance (Eq. [33]) using the zonally averaged geopotential gradient and multiplying the square root by –1.

obtained by cyclostrophic equilibrium. The profile shows an equatorial maximum of ~90 m s^{-1}, which is within the range of observations; however, the two observed mid-latitude maxima in each hemisphere are not reproduced by the model.

The computed meridional profiles of the global mean north-south wind at this height agree with the dominant direction observed in each hemisphere; that is, negative towards the southern hemisphere and positive towards the northern hemisphere. Its magnitude is only ~3 m s^{-1}, while the observed magnitude is ~10 m s^{-1}. However, at night, when the Sun has warmed the surface, the meridional wind moves from the poles to the equator, and the calculated meridional profile shows greater agreement with the observed profile (Fig. 11).

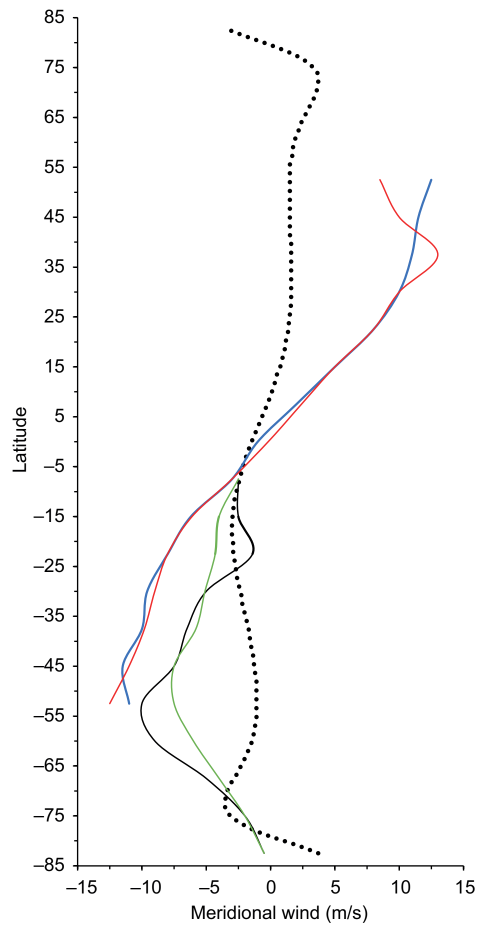

Fig. 11. Meridional profiles of the mean north-south wind as measured at the upper cloud level (65-70 km): Pioneer Venus, 1979-1983 (blue line); Galileo, 1990 (red line); Venus Express VIRTIS, 2006-2012 (black line); Venus Express VMC, 2006-2012 (green line). These curves were obtained from Fig. 5 in Sánchez-Lavega et al. (2017). The global mean meridional profile of the north-south wind at 68.5 km altitude is given as computed by the model (dotted curve).

The global daily average zonal wind profile (Fig. 12) computed by the model is within the range of the corresponding observations. Below the level at which

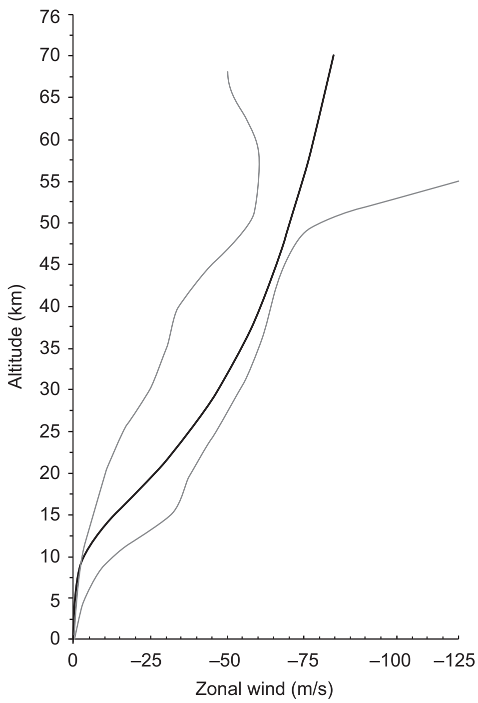

Fig. 12. The shaded area contains the observed vertical profiles of the zonal wind by the Pioneer-Venus and Venera probes 8, 9, 10, and 12. The black curve corresponds to the profile calculated by our model globally averaged on the last Venusian day (day 300).

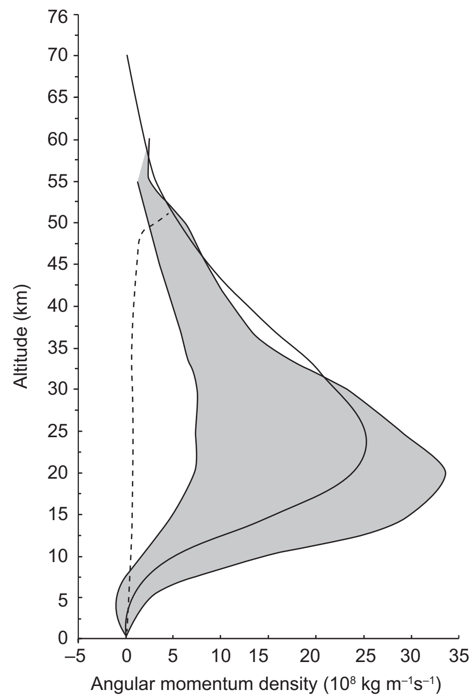

Fig. 13. Angular momentum density $\rho^*\ U^*$ acosφ (10^8 kgm^{-1} s^{-1}) as a function of height. The gray area contains the profiles obtained from zonal wind and atmospheric density measurements by the four Pioneer Venus probes. The solid black curve is obtained from the zonal wind and atmospheric density computed by the model. The dashed curve corresponds to the VMTZ experiment where the vertical transport terms of specific momentum $\omega^*_\zeta \frac{\partial U^*}{\partial \zeta^*}$ and $\omega^*_\zeta \frac{\partial V^*}{\partial \zeta^*}$, in movement Eqs. (28) and (29), have been despised.

approximately half of the atmospheric mass is contained, the average computed zonal wind is close to zero and becomes relevant above 10 km. At 35 km, the computed wind reaches a speed of ~55 m s^{-1}, and at 70 km, it reaches ~77 m s^{-1}, 42.7 times the rotation velocity of the planet at the equator.

The angular momentum density profiles obtained from the zonal wind and atmospheric density in the four Pioneer Venus probes (Schubert et al., 1980) are located within the gray area of Figure 13. The Sounder probe near the equator and the Day and Night probes in tropical latitudes show a maximum at 20 km altitude, which is reflected in the right edge of the shaded area while the North probe at high latitudes shows a maximum at ~25 km altitude. The model profile (solid black curve), which is a global average of the last Venusian day (day 300), has a maximum at ~23 km altitude. This figure shows that above 70 km altitude, the contribution of the angular momentum density to the computed relative angular momentum Mr of the entire atmosphere can be neglected, which explains why the value we obtain for Mr of 3.2×10^{28} kg m^2 s^{-1} in the troposphere is within the range given by Golitsyn (1984). The comparison in Figure 13 between the solid curve and the dashed curve obtained from the experiment VMTZ, suggests that the vertical transport of specific momentum in the motion equation (Eqs. [28] and [29]), plays an important role in maintaining the zonal circulation between the surface and the cloud base at ~48 km altitude, overcoming vertical turbulent friction with the surface. Above the cloud base, superrotation is maintained mainly by the force associated with the meridional gradient of the geopotential, even without a specific moment's vertical contribution.

6. Discussion: thermal gradients as primary forcing in the context of superrotation theories

Our results identify horizontal temperature gradients—derived from a thermodynamic model—as the principal forcing factor for superrotation in slowly rotating planets, offering a perspective that complements and synthesizes several mechanisms proposed in the literature.

Traditionally, explanations for superrotation on Venus and Titan have focused on momentum-transport mechanisms driven by waves (gravity, tidal, or Rossby waves) and turbulence, which balance the meridional flow (Read and Lebonnois, 2018). Our work does not contradict these mechanisms but proposes a more fundamental origin for momentum injection: direct thermal forcing. In essence, day-night and equator-pole gradients, sustained by high thermal inertia and slow rotation, generate a robust ageostrophic circulation in cyclostrophic balance. This idea connects directly to the work of Peng and Mitchell (2014), who demonstrated that an ageostrophic instability, fed by such gradients, can be an efficient engine for accelerating zonal winds to superrotating states without the need for topographic forcing.

This approach also sheds light on the apparent rarity of robust superrotation among the solar system's planets. The key lies in the unique dynamical regime created by slow rotation. As Laraia and Schneider (2015) insightfully discuss in a broader context, the transition to a superrotating state is favored when the planetary rotational constraint is weak. Crucially, this corresponds to a large Rossby number regime. Venus, with its exceedingly long sidereal day, epitomizes this regime. Here, inertial and advective forces dominate the Coriolis force, allowing significant deviations from geostrophic balance and facilitating the organization of flow by large-scale thermal gradients rather than by rotation.

Our thermodynamic model directly quantifies the second essential ingredient in this weak-rotation regime: thermal forcing. A large Rossby number is necessary but not sufficient. Superrotation also requires that radiative processes permit the establishment of large-scale, sustained horizontal temperature gradients. On a rapidly rotating planet like Earth, the strong Coriolis force efficiently organizes such thermal contrasts into geostrophically balanced mid-latitude jets, suppressing the mean meridional overturning needed for superrotation. In contrast, on a slow rotator like Venus, the weak rotational constraint allows intense diurnal and hemispheric heating contrasts—calculated by our model—to drive a powerful, direct thermal circulation. This ageostrophic flow, operating in a high-Rossby-number environment, becomes the primary agent for the upward and poleward transport of angular momentum.

We refined the paradigm: the superrotation regime arises from the confluence of a weak rotational constraint (high Rossby number) and powerful, sustained thermal gradients. Our work provides the thermodynamic basis for this second condition, showing that Venus' combination of an exceptionally long solar day (~117 Earth days), which drives meridional and day-night heating contrasts, and high thermal inertia creates the necessary thermal forcing. This forcing then acts through ageostrophic dynamics—either through a direct mean circulation or through instabilities, as in Peng and Mitchell (2014)—to accelerate the zonal flow, which is subsequently shaped and maintained by wave-driven processes (Read and Lebonnois, 2018).

Thus, we situate our findings within a unifying framework: in slowly rotating bodies, meridional and diurnal thermal gradients—thermodynamically computed by our model—act as the primary forcing that initiates and sustains superrotation, while wave and mixing mechanisms provide the necessary coupling and redistribution to establish and maintain the global atmospheric jet.

7. Summary and conclusions

Seventy-six percent of the solar radiation that reaches Venus' atmosphere is reflected into space mainly by the cloud layer. Only 24% penetrates the atmosphere, where most of it is absorbed by the clouds (16%), followed by the atmosphere (4.8%) and a small part by the surface of the regolith (3.2%); however, the heavy atmosphere of the planet, constituted mainly by CO_2, behaves almost like a black body for longwave radiation, so that in thermodynamic equilibrium, the surface temperature reaches the average value of ~745 K (472 ºC), being this the most prominent solution of the model.

The main mechanism of heat transport in the Venusian troposphere in our model is horizontal, planetary-scale eddy turbulent heat transport, which mainly smooths the meridional temperature gradient. After performing several sensitivity experiments, we found that the turbulent exchange coefficient required in our solution is equal to 4.5×10^5 m^2 s^{-1}, one order of magnitude lower than that used for the Earth's troposphere (Schubert et al., 1980). The incorporation of thermal energy advection is an important component of the energy budget that contributes to the smoothing and redistribution of the meridional temperature gradient, which can improve the results.

We have assumed a constant lapse rate in the troposphere in hydrostatic equilibrium; therefore, using the equation of state, we have expressed the geopotential as a function of pressure (a vertical coordinate) and the atmospheric temperature field at the surface (Eq. [5]). The result means that the geopotential increases with height, starting from zero at the surface, where $p_s = 9.2 \times 10^6$ Pa, and reaching a typical value of 6.21×10^5 m^2 s^{-2} (computed with T_{S0} = 737 K) at the top of the troposphere, where $p = 3.6 \times 10^3$ Pa. The gradient of the geopotential increases the acceleration of the specific momentum with height. A steady state is achieved at each level due to the balance between the gradient of the geopotential, the vertical turbulent stress in the PBL, and the divergence of the horizontal turbulent transport of momentum. This transport occurs against the momentum gradient, which is parameterized in the model using a viscosity coefficient ($v = 1.2 \times 10^7$ m^2 s^{-1}).

Above 10 km altitude, the average zonal wind exceeds the rotation velocity of the planet at the equator (superrotation). According to Figure 6a, at the upper level of the clouds, the superrotation of the zonal wind manifests with a prograde zonal wind of ~85 km s^{-1} in lower latitudes. The vertical transport of specific momentum in the equations of motion plays an essential role in maintaining the zonal circulation between the surface and the cloud base at ~48 km altitude, overcoming vertical turbulent friction at the surface. Above the cloud base, superrotation is maintained mainly by the force associated with the meridional gradient of the geopotential, even without the vertical transport contribution of a specific moment. In this way, the theoretical solution of the equations of motion predicts the position and intensity of mid-latitude prograde jets (35º N and 35º S) between the day and night side at ~90º E. These mid-latitude jets are present in the meridional profile of the observed zonal wind in Figure 10.

Thermal tides are fluctuations in the temperature field that occur in response to solar heating near the equator. These fluctuations manifest as waves in the thermal field that propagate vertically and horizontally through the atmosphere, transporting heat from warm to relatively cold regions, redistributing thermal energy, and smoothing its gradients. According to Horinouchi et al. (2020), thermal tides help balance heat transfer and angular momentum redistribution, stabilizing and maintaining superrotation at the cloud level.

The agreement of our results with the observations leads us to conclude that the diurnal thermal tide associated with the west-east advance of solar heating at the surface, manifested in the temperature field T_S and consequently in the zonal and meridional gradients of the geopotential, is the main force that generates and maintains the superrotation of the atmosphere.

It is not necessary to perform a radiative-convective adjustment process in the model because the lapse rate is prescribed to be constant throughout the troposphere. In a radiative-convective adjustment process, vertical heat transfer by thermal tides may also play an important role. In our model the constant lapse rate determines the vertical profile of the geopotential by being part of the coefficient ($1\ \gamma^{-1}$) and the exponent ($R\gamma$) in Eq. (5), consequently the advance of solar heating at the surface, associated with the diurnal thermal tide, is also manifested at the cloud level, establishing the superrotation at that level. However, Fukuya et al. (2021) found that semidiurnal tides are predominant around cloud tops, while our results are dominated by diurnal tides at this level.

As a final remark, the essential aspect of our thermodynamic model consists in the fact that the dynamic part of the superrotation of the atmosphere of Venus is subordinated to the temperature field, that is, the solution of the equations of conservation of thermal energy in the atmosphere and the surface of the regolith.

Data availability

The thermodynamic model of Venus code and results are available in https://zenodo.org/records/8432706 (Mendoza et al., 2024).

Figures 2, 3, 7, 8, and 9 were made with Panoply v. 5.4 developed by NASA Goddard Institute for Space Studies, available at https://www.giss.nasa.gov/tools/panoply/download/.

Acknowledgments

The authors thank Enrique Ortiz for his valuable support with the software and figure preparation; Pedro Damián Cruz Santiago for his technical support and for enabling local computational resources to run the model; and UNAM-Amazon Web Services for the computational resources and advice provided to carry out this project.

References

Adem J. 1962. On the theory of the general circulation of the atmosphere. Tellus A: Dynamic Meteorology and Oceanography 14: 102-115. https://doi.org/10.3402/tellusa.v14i1.9532

Adem J. 1965. Preliminary model computing mid-tropospheric and surface temperature from satellite data. Journal of Geophysical Research 70: 2763-2767. https://doi.org/10.1029/JZ070i012p02763

Adem J. 1970. Incorporation of advection of heat by mean winds and by ocean currents in a thermodynamic model for long-range weather prediction. Monthly Weather Review 98: 776-786. https://doi.org/10.1175/1520-0493(1970)098<0776:IOAOHB>2.3.CO;2

Archinal BA, Acton CH, A'Hearn MF, Conrad A, Consolmagno GJ, Duxbury T, Hestroffer D, Hilton JL, Kirk RL, Klioner SA, McCarthy D, Meech K, Oberst J, Ping J, Seidelmann PK, Tholen DJ, Thomas PC, Williams IP. 2018. Report of the IAU Working Group on Cartographic Coordinates and Rotational Elements: 2015. Celestial Mechanics and Dynamical Astronomy 130: 22. https://doi.org/10.1007/s10569-017-9805-5

Cohen M, Holmes J, Lewis S, Patel M, Lebonnois S. 2025. Three worlds in one: Venus as a natural laboratory for the effect of rotation period on atmospheric circulation. The Astrophysical Journal Letters 980: L11. https://doi.org/10.3847/2041-8213/adade9

Fels SB, Lindzen RS. 1974. The interaction of thermally excited gravity waves with mean flows. Geophysical Fluid Dynamics 6: 149-191. https://doi.org/10.1080/03091927409365793

Fujisawa Y, Murakami S, Sugimoto N, Takagi M, Imamura T, Horinouchi T, Hashimoto GL, Ishiwatari M. Enomoto T, Miyoshi T, Kashimura H, Hayashi YY. 2022. The first assimilation of Akatsuki single-layer winds and its validation with Venusian atmospheric waves excited by solar heating. Science Reports 12: 14577. https://doi.org/10.1038/s41598-022-18634-6

Fukuya K, Imamura T, Taguchi M, Fukuhara T, Kouyama T, Horinouchi T, Peralta J, Futaguchi M, Yamada T, Sato TM, Yamazaki A, Murakami SY, Satoh T, Takagi M, Nakamura M. 2021. The nightside cloud-top circulation of the atmosphere of Venus. Nature 595: 511-515. https://doi.org/10.1038/s41586-021-03636-7

Gierasch, PJ 1975. Meridional circulation and the maintenance of the Venus atmospheric rotation. Journal of the Atmospheric Sciences 32: 1038-1044. https://doi.org/10.1175/1520-0469(1975)032<1038:MCATMO>2.0.CO;2

Gierasch PJ, Goody R, Young R, Crisp D, Edwards C, Kahn R. 1997. The general circulation of the Venus atmosphere: An assessment. In: Venus II: Geology, geophysics, atmosphere, and solar wind environment (Bougher SW, Hunten DM, Phillips RJ, Matthews MS, Ruskin AS, Guerrieri ML, Eds.). University of Arizona Press, Tucson, USA, 459-500. https://doi.org/10.2307/j.ctv27tct5m.19

Golitsyn GS, 1984. Some problems of Venus' atmospheric dynamics. Icarus 60: 289-306. https://doi.org/10.1016/0019-1035(84)90190-8

Gulkis S, Pater ID. 2003. Radio astronomy, planetary. In: Encyclopedia of physical science and technology. 3rd ed. (Meyers RA, Ed.). Academic Press, 687-712. https://doi.org/10.1016/B0-12-227410-5/00637-2

Horinouchi T, Hayashi YY, Watanabe S, Yamada M, Yamazaki A, Kouyama T, Taguchi M, Fukuhara T, Takagi M, Ogohara K, Murakami S, Peralta J, Limaye SS, Imamur T, Nakamura M, Sato TM, Satoh T. 2020. How waves and turbulence maintain the super-rotation of Venus' atmosphere. Science 368: 405-409. https://doi.org/10.1126/science.aaz4439

Kouyama T, Taguchi M, Fukuhara T, Imamura T, Horinouchi T, Sato TM, Murakami S, Hashimoto GL, Lee YJ, Futaguchi M, Yamada T, Akiba M, Satoh T, Nakamura M. 2019. Global structure of thermal tides in the upper cloud layer of Venus revealed by LIR on board Akatsuki. Geophysical Research Letters 46: 9457-9465. https://doi.org/10.1029/2019GL083820

Laraia AL, Schneider T. 2015. Superrotation in terrestrial atmospheres. Journal of the Atmospheric Sciences 72: 4281-4296. https://doi.org/10.1175/JAS-D-15-0030.1

Lebonnois S, Hourdin F, Eymet V, Crespin A, Fournier R, Forget F. 2010. Superrotation of Venus' atmosphere analyzed with a full general circulation model. Journal of Geophysical Research: Planets 115: E06006. https://doi.org/10.1029/2009JE003458

Lebonnois S, Lee C, Yamamoto M, Dawson J, Lewis SR, Mendonca J, Read P, Parish HF, Schubert G, Bengtsson L, Grinspoon D, Limaye SS, Schmidt H, Svedhem H, Titov DV. 2013. Models of Venus atmosphere. In: Towards understanding the climate of Venus (Bengtsson L, Bonnet RM, Grinspoon D, Koumoutsaris S, Lebonnois S, Titov D., Eds.). ISSI Scientific Report Series 11. Springer, New York, 159-156. https://doi.org/10.1007/978-1-4614-5064-1_8

Lee C, Lewis SR, Read PL. 2007. Superrotation in a Venus general circulation model. Journal of Geophysical Research 112: E04S11. https://doi.org/10.1029/2006JE002874

Lefèvre M. 2022. Venus boundary layer dynamics: Eolian transport and convective vortex. Icarus 387: 115167. https://doi.org/10.1016/j.icarus.2022.115167

Lorenz RD. 2016. Surface winds on Venus: Probability distribution from in-situ measurements. Icarus 264: 311-315. https://doi.org/10.1016/j.icarus.2015.09.036

Lorenz RD, Crisp D, Huber L. 2018. Venus atmospheric structure and dynamics from the VEGA lander and balloons: New results and PDS archive. Icarus 305: 277-283. https://doi.org/10.1016/j.icarus.2017.12.044

Matsuda Y. 1980. Dynamics of the four-day circulation in the Venus atmosphere. Journal of the Meteorological Society of Japan, Series II 58: 443-470. https://doi.org/10.2151/jmsj1965.58.6_443

Matsuda Y, 1982. A further study of dynamics of the four-day circulation in the Venus atmosphere. Journal of the Meteorological Society of Japan, Series II 60: 245-254. https://doi.org/10.2151/jmsj1965.60.1_245

Matsuda Y. 2010. Dynamics of the super-rotation of Venus atmosphere. Lecture presented at the CPS International School of Planetary Sciences, Kobe, Japan (January 1).

Mendonça JM, Read PL. 2016. Exploring the Venus global super-rotation using a comprehensive general circulation model. Planetary and Space Science 134: 1-18. https://doi.org/10.1016/j.pss.2016.09.001

Mendonça JM, Buchhave LA. 2020. Modelling the 3D climate of Venus with OASIS. Monthly Notices of the Royal Astronomical Society 496: 3512-3530. https://doi.org/10.1093/mnras/staa1618

Mendoza VM, Villanueva EE, Garduño R, Sánchez-Meneses O. 2017. Atmospheric emissivity with clear sky computed by E-Trans/HITRAN. Atmospheric Environment 155: 174-188. https://doi.org/10.1016/j.atmosenv.2017.01.048

Mendoza VM, Mendoza B, Garduño R, Cordero G, Pazos M, Cervantes S, Cervantes K. 2021. Thermodynamic simulation of the seasonal cycle of temperature, pressure and ice caps on Mars. Atmósfera 34: 1-23. https://doi.org/10.20937/atm.52747

Mendoza VM, Mendoza B, Pazos-Espejel M, Quintanar A, Garduño R. 2023. Super rotation of the Venus atmosphere computed with a thermodynamic model. Zenodo. https://doi.org/10.5281/ZENODO.8432706

Milanković M. 1920. Théorie mathématique des phénomènes thermiques produits par la radiation solaire. Académie Yougoslave des Sciences et des Arts de Zagreb. Gauthier-Villars, Paris, France, 340 pp.

Mogul R, Zolotov MY, Way MJ, Limaye SS. 2025. Re-analysis of Pioneer Venus data: Water, iron sulfate, and sulfuric acid are major components in Venus' aerosols. Journal of Geophysical Research: Planets 130: e2024JE008582. https://doi.org/10.1029/2024JE008582

Moroz VI, Ekonomov AP, Moshkin BE, Revercomb HE, Sromovsky LA, Schofield JT, Spänkuch D, Taylor FW, Tomasko MG. 1985. Solar and thermal radiation in the Venus atmosphere. Advances in Space Research 5: 197-232. https://doi.org/10.1016/0273-1177(85)90202-9

Moroz VI, Zasova LV. 1997. VIRA-2: A review of inputs for updating the Venus international reference atmosphere. Advances in Space Research 19: 1191-1201. https://doi.org/10.1016/S0273-1177(97)00270-6

Petropoulos B, Telonis P. 1993. Physical parameters of the atmosphere of Venus from Venera 15 and 16 missions. Earth, Moon, and Planets 63: 1-7. https://doi.org/10.1007/BF00572133

Peng W, Mitchell JL. 2014. Planetary ageostrophic instability leads to superrotation. Geophysical Research Letters 41: 4118-4126. https://doi.org/10.1002/2014GL060345

Read PL, Lebonnois S. 2018. Superrotation on Venus, on Titan, and elsewhere. Annual Review of Earth and Planetary Sciences 46: 175-202. https://doi.org/10.1146/annurev-earth-082517-010137

Rossow WB, Williams GP. 1979. Large-scale motion in the Venus stratosphere. Journal of the Atmospheric

Sciences 36: 377-389. https://doi.org/10.1175/1520-0469(1979)036<0377:LSMITV>2.0.CO;2

Rothman LS, Gordon IE, Barbe A, Benner DC, Bernath PF, Birk M, Boudon V, Brown LR, Campargue A, Champion J-P, Chance K, Coudert LH, Dana V, Devi VM, Fally S, Flaud J-M, Gamache RR, Goldman A, Jacquemart D, Kleiner I, Lacome N, Lafferty WJ, Mandin J-Y, Massie ST, Mikhailenko SN, Miller CE, Moazzen-Ahmadi N, Naumenko OV, Nikitin AV, Orphal J, Perevalov VI, Perrin A, Predoi-Cross A, Rinsland CP, Rotger M, Šimečková M, Smith MAH, Sung K, Tashkun SA, Tennyson J, Toth RA, Vandaele AC, Vander Auwera J. 2009. The HITRAN 2008 molecular spectroscopic database. Journal of Quantitative Spectroscopy and Radiative Transfer 110: 533-572. https://doi.org/10.1016/j.jqsrt.2009.02.013

Saltzman B. 1978. A survey of statistical-dynamical models of the terrestrial climate. Advances in Geophysics 20: 183-304. https://doi.org/10.1016/S0065-2687(08)60324-6

Sánchez-Lavega A, Lebonnois S, Imamura T, Read P, Luz D. 2017. The atmospheric dynamics of Venus. Space Science Reviews 212: 1541-1616. https://doi.org/10.1007/s11214-017-0389-x

Schubert G, Whitehead JA. 1969. Moving flame experiment with liquid mercury: Possible implications for the Venus atmosphere. Science 163: 71-72. https://doi.org/10.1126/science.163.3862.71

Schubert G, Covey C, Genio AD, Elson LS, Keating G, Seiff A, Young RE, Apt J, Counselman CC III, Kliore AJ, Limaye SS, Revercomb HE, Sromovsky LA, Suomi VE, Taylor F, Woo R, von Zahn U. 1980. Structure and circulation of the Venus atmosphere. Journal of Geophysical Research: Space Physics 85: 8007-8025. https://doi.org/10.1029/JA085iA13p08007

Stevens B, Duan J, McWilliams JC, Münnich M, Neelin JD. 2002. Entrainment, Rayleigh friction, and boundary layer winds over the tropical Pacific. Journal of Climate 15: 30-44. https://doi.org/10.1175/1520-0442(2002)015<0030:ERFABL>2.0.CO;2

Sugimoto N, Takagi M, Matsuda Y. 2019. Fully developed superrotation driven by the mean meridional circulation in a Venus GCM. Geophysical Research Letters 46: 1776-1784. https://doi.org/10.1029/2018GL080917

Sugimoto N, Fujisawa Y, Komori N, Kashimura H, Takagi M, Matsuda Y. 2023. Super-rotation independent of horizontal diffusion reproduced in a Venus GCM. Earth, Planets and Space 75: 44. https://doi.org/10.1186/s40623-023-01806-7

Takagi M, Matsuda Y. 2007. Effects of thermal tides on the Venus atmospheric superrotation. Journal of Geophysical Research: Atmospheres 112: D09112. https://doi.org/10.1029/2006JD007901

Takagi M, Sugimoto N, Ando H, Matsuda Y, 2018. Three-dimensional structures of thermal tides simulated by a Venus GCM. Journal of Geophysical Research: Planets 123: 335-352. https://doi.org/10.1002/2017JE005449

Takahashi YO, Hayashi YY, Hashimoto GL, Kuramoto K, Ishiwatari M, Kashimura H. 2024. Dependence of the radiative-convective equilibrium structure of the lower atmosphere of Venus on the thermodynamic model. Journal of the Meteorological Society of Japan, Series II 102: 5-16. https://doi.org/10.2151/jmsj.2024-001

Taylor FW, Hunten DM. 2014. Chapter 14. Venus: Atmosphere. In: Encyclopedia of the Solar System (Spohn T, Breuer D, Johnson TV, Eds.). 3rd ed. Elsevier, 305-322. https://doi.org/10.1016/B978-0-12-415845-0.00014-1

Thompson PD. 1961. Numerical weather analysis and prediction. The Macmillan Company, New York

Titov DV, Bullock MA, Crisp D, Renno NO, Taylor FW, Zasova LV. 2007. Radiation in the atmosphere of Venus. In: Exploring Venus as a terrestrial planet (Esposito LW, Stofan ER, Cravens TE, Eds.). Geophysical Monograph Series 176: 121-138. https://doi.org/10.1029/176GM08

Vidmachenko AP. 2025. The main astronomical and physical characteristics of Venus and their comparison with Earth. In: The influence of volcanic activity on the formation of the Venus surface (Vidmachenko AP, Ovsak OS, Kuznetzova JG, Steklov OF, Eds.). International Science Group, 8-28. https://doi.org/10.46299/979-8-89814-227-8.1

Yamamoto M, Takahashi M. 2003a. The fully developed superrotation simulated by a general circulation model of a Venus-like atmosphere. Journal of the Atmospheric Sciences 60: 561-574. https://doi.org/10.1175/1520-0469(2003)060<0561:TFDSSB>2.0.CO;2

Yamamoto M, Takahashi M. 2003b. Superrotation and equatorial waves in a T21 Venus-like AGCM. Geophysical Research Letters 30: 1449. https://doi.org/10.1029/2003GL016924

Yamamoto M, Takahashi M. 2007. Simulations of superrotation using a GCM for Venus' middle atmosphere. Earth, Planets and Space 59: 971-979. https://doi.org/10.1186/BF03352036